NJC

ROYAL SOCIETY OF CHEMISTRY

PAPER

View Article Online
View Journal



Cite this: DOI: 10.1039/d6nj00633g

# Visible light degradation of tetracycline and bisphenol A by a hybrid photocatalyst composed of orange peel biochar, clay, and C/N-doped titania

Morenike O. Adesina,*[abcd] Moses O. Alfred,[abc] Harshadrai M. Rawel,[e] Christina Günter,[f] Anne Nitschke,[a] Jiyong Kim,[g] Armin Wedel,[g] Wouter Koopman,[h] Martins O. Omorogie,[abc] Emmanuel I. Unuabonah †[bc] and Andreas Taubert *[a]

A new photoactive nitrogen-doped hybrid clay photocatalyst based on orange peel, titania, and melamine is highly effective for the degradation of tetracycline (TET) and bisphenol A (BPA) from aqueous solution. The photocatalysts were synthesized using a simple low cost approach and characterized by powder X-ray diffraction, scanning electron microscopy, nitrogen sorption, thermogravimetric analysis, UV-visible diffuse reflectance spectroscopy, and X-ray photoelectron spectroscopy (XPS). The titania present in the material is C/N-doped and plays a key role in the photocatalytic process, influencing the bandgap and the overall optical properties of the hybrid photocatalyst. Notably, XPS confirms the successful incorporation of nitrogen into the $TiO_2$ lattice. This N-doping induces a red shift in the absorption edge of the photocatalysts, which significantly improves the photocatalytic efficiency under visible light irradiation relative to pristine $TiO_2$. The photocatalysts also exhibit an increased specific surface area, reaching up to 180 $m^2\ g^{-1}$. Under visible light irradiation at 25 °C and neutral pH, the photocatalysts achieve complete degradation of TET in aqueous solutions within 30 min. Similarly, 82% degradation of BPA in 10 mg $L^{-1}$ BPA aqueous solutions is achieved within 120 min. Total organic carbon analysis reveals moderate mineralisation of 46 to 50% for both pollutants and radical trapping experiments identify superoxide radicals ($^{\bullet}O_2^-$) as the primary reactive species responsible for pollutant degradation. Furthermore, the catalysts show an excellent performance in the degradation of TET in river water, clearly demonstrating an applicability in practical water treatment. Finally, the photocatalysts can effectively be recycled without significant loss of efficiency.

Received 19th February 2026,
Accepted 14th May 2026

DOI: 10.1039/d6nj00633g

rsc.li/njc



## 1. Introduction

The presence of emerging contaminants (ECs) like pharmaceuticals and endocrine disruptors in aquatic environments is a global issue. This is due to the potential adverse effects on human health and natural ecosystems caused by these compounds.[1,2] Tetracycline (TET) and bisphenol A (BPA) are typical contaminants found in environmental water bodies. They primarily originate from bacterial control and industrial manufacturing, respectively.[3,4] TET concentrations vary widely across regions and aqueous matrices, ranging from 0 to 263.6 ng $L^{-1}$.[5,6] Similarly, BPA levels can reach 0.37 to 17.2 mg $L^{-1}$ in landfill leachate and paper recycling effluents.[6] Both compounds pose serious threats to all life forms because they bioaccumulate and cause reproductive toxicity.[1,2]

Among others, adsorption,[7,8] membrane treatment,[9–11] biological treatment,[11,12] and advanced oxidation processes[13,14] are currently used for the removal of ECs. Among these, photocatalysis is especially promising due to its high efficiency, eco-friendliness, low cost, and mild reaction conditions.[15,16] Although numerous photocatalysts have been reported for water treatment,[14] there is an increasing need for cheap, yet

[a] Institute of Chemistry, University of Potsdam, D-14476 Potsdam, Germany. E-mail: adesina9856@run.edu.ng, ataubert@uni-potsdam.de
[b] African Centre of Excellence for Water and Environmental Research (ACEWATER), Redeemer's University, PMB 230, 232101 Ede, Nigeria
[c] Department of Chemical Sciences, Redeemer's University, PMB 230, 232101 Ede, Nigeria
[d] Department of Chemical Sciences, Lead City University, 200005 Ibadan, Nigeria
[e] Institute of Nutritional Science, University of Potsdam, D-14558 Nuthetal Potsdam, Germany
[f] Institute of Geosciences, University of Potsdam, D-14476 Potsdam, Germany
[g] Functional Materials and Devices, Fraunhofer Institute for Applied Polymer Research IAP, Potsdam, D-14476 Potsdam, Germany
[h] Institute of Physics and Astronomy, University of Potsdam, D-14476 Potsdam, Germany
† E.I.U. deceased on March 26, 2025.

highly efficient, durable, and multi-functional photocatalysts for point-of-use application in low-income and developing countries.

$TiO_2$ nanoparticles are widely used for the photocatalytic degradation of contaminants in water and are considered one of the most effective photocatalytic materials due to their unique optical and electronic properties, chemical stability, and biocompatibility.[16,17] However, they face limitations due to strong agglomeration and quick recombination of photogenerated electron–hole pairs. Moreover, their photocatalytic activity is limited to UV light because of their large band gap.[18,19] To address these issues, various modification strategies have been proposed, such as immobilization on different supports,[20] doping,[21,22] or the addition of co-catalysts.[23,24]

Various substrates have been used as catalyst supports, including graphene,[25,26] cellulose membranes,[27] alumina clays,[28] carbonaceous materials,[24,29] or a combination thereof.[30,31] Loading $TiO_2$ onto a support reduces the likelihood of agglomeration; this is important as agglomeration negatively affects the photocatalytic process and should therefore be avoided. Moreover, many supports also exhibit a good adsorption capacity for pollutants; this increases the concentration of pollutants around the $TiO_2$, which in turn further boosts the activity of the photocatayst.[13,32]

The combination of adsorption and photodegradation is particularly beneficial because the concentration of most relevant pollutants is often on the parts per million (ppm) level or less. Adsorption onto the photocatalyst surface thus increases the rate of photooxidation and concurrent photodegradation of the pollutants. Additionally, some supports facilitate fast and easy photocatalyst recovery and reuse.

However, the high cost of some support materials like graphene oxide, carbon nanotubes, and commercial activated carbon limits their practical application as $TiO_2$ carriers. Recently, biochar has emerged as a cost-effective alternative for this purpose. Converting agrowaste such as orange peels, corn cobs, peanut shells, *etc.* to a porous biochar not only provides a sustainable catalyst support but also transforms organic waste into a useful material.

Titania-based biochar composites have indeed shown high stability and promising photocatalytic performance for the degradation of various organic pollutants. For example, Thuan *et al.* optimized a $TiO_2$/rice husk biochar composite for BPA removal, achieving excellent photocatalytic BPA degradation.[33] Similarly, Lazarotto *et al.* employed spent coffee ground biochar with immobilized $TiO_2$ for diclofenac degradation, attaining 90% removal efficiency.[34] Ashebir *et al.* developed N-doped $TiO_2$/Prosopis Juliflora biochar nanocomposites for ciprofloxacin degradation, reaching degradation efficiencies of 98.9% under UV light and 96.9% under visible light.[35]

Moreover, introducing non-metal elements such as nitrogen (N), carbon (C), or sulphur (S) into $TiO_2$ is an effective approach to improve the optical absorption and photocatalytic efficiency of $TiO_2$ in the visible region.[21,36] The main ways of incorporating these elements into the $TiO_2$ lattice are interstitial doping or substitutional doping.[37] Nitrogen is particularly attractive as a dopant due to its atomic size, which is similar to oxygen, low ionization energy, and high stability.[38]

Nitrogen doping modifies the electronic structure of $TiO_2$ by introducing N 2p states above the valence band or by narrowing the band gap through orbital mixing with O 2p states. This leads to a red-shift in the absorption edge, enabling visible-light activation. In addition, N doping can improve charge carrier dynamics by suppressing the recombination of photogenerated charges, thereby enhancing the overall quantum efficiency of the photocatalytic process.[38,39] Additionally, co-doping with two or more non-metals can create synergistic effects to further reduce the $TiO_2$band gap. This results in a further red-shift of the absorption edge and an enhanced charge separation, which leads to an overall higher photocatalytic activity compared to pure $TiO_2$.[37]

In the quest for simpler and greener methods for nanomaterial synthesis with improved photo-conversion properties, this study explores nitrogen-containing hybrid clay composites as a substrate for the immobilization of $TiO_2$ nanoparticles. These composites serve a dual purpose as a substrate for $TiO_2$ and as a source of non-metal elements, *i.e.*, C and N, for incorporation into the $TiO_2$ photocatalyst lattice. The support composite material is made from kaolin clay, orange peel, and melamine, and is combined with titania to produce a new $TiO_2$ hybrid clay photocatalyst. Orange peel was chosen for its high lignocellulose content, natural surface functional groups, availability, and ability to produce porous carbonaceous materials.[40] Melamine was selected for its high nitrogen content (66%), easy and safe handling, and limited side reactions during doping compared to other nitrogen sources like urea or ammonia.[41]

A previous study has already demonstrated the presence of Ti–O–C and Ti–C bonds in an orange peel biochar/clay/$TiO_2$ composite using X-ray photoelectron spectroscopy (XPS). This suggests that some carbon from the biochar can be integrated into the $TiO_2$ lattice.[42] The addition of C to the $TiO_2$ lattice appears to tune the $TiO_2$ bandgap (among other factors), resulting in new catalyst composites with lower band gap energies than the one of pure $TiO_2$ (*ca.* 3.20 eV).[28] Under natural sunlight, these orange peel biochar/clay/$TiO_2$ composites demonstrate good photocatalytic efficiency for the degradation of TET.[42]

In this current study, we evaluate a group of new nitrogen-doped hybrid clay/$TiO_2$ composites for the photocatalytic degradation of TET and BPA under visible light. The materials differ profoundly from the previous catalysts[31,42] in some selected aspects but are again highly effective photocatalysts for the degradation of TET and BPA.

## 2. Materials and methods

Titanium(IV) isopropoxide ($Ti(OCH(CH_3)_2)_4$, TTIP), tetracycline (98%, all Sigma-Aldrich), bisphenol A (98%), melamine (analytical grade), anhydrous ethanol (99.8%, all from Carl Roth), and isopropanol (70%, Sigma Aldrich) were used as received. Deionized (DI) water was used for all experiments. Additional

 

comparison experiments were conducted using river water collected from the Nuthe River (52°23′43″N, 13°4′13″E) at the Nuthebrücke (Humboldtring) in D-14482 Potsdam, Germany, in 250 mL amber bottles, following the legal regulations of the State of Brandenburg on water collection from public surface waters (§25 Wasserhaushaltsgesetz). The samples were promptly transferred to the laboratory, stored at 4 °C, and used within 24 h of collection. Raw kaolin clay was sourced from Redemption City, Mowe (6°48′0″N, 3°26′0″E.), Ogun State, Nigeria. Orange peel (OP) was obtained from the local REWE supermarket in D-14476 Potsdam-Golm, Germany, dried, and ball-milled as previously described.[31]

### 2.1. Preparation of N-doped hybrid clay composite

A combination of kaolin clay, orange peel powder, and melamine in a 1 : 1 : 5 weight ratio was ground and mixed using mortar and pestle until a macroscopically homogenous mixture was obtained. The mixture was placed in a muffle furnace and calcined in air, heated at 5 °C $min^{-1}$ to reach the final calcination temperature of 300 °C. Calcination times at 300 °C were 1, 2, or 3 h. Calcination at 300 °C was chosen to initiate biomass carbonization and melamine decomposition for N-doping, while limiting structural changes and total loss of surface functionalities in the hybrid matrix; higher-temperature treatments would complete carbonization, increase porosity, and enhance nitrogen integration into the $TiO_2$.[43,44]

The nitrogen-doped hybrid clay composites obtained from this synthesis are labelled N-OPK1, N-OPK2, and N-OPK3, respectively, where N refers to (nitrogen from) melamine, OP refers to orange peel, K refers to kaolin clay, and the numbers 1, 2, or 3 refer to the calcination time in hours. To assess the influence of the nitrogen source, a composite without melamine, denoted as OPK, was prepared at 300 °C for 2 h again using a heating ramp of 5 °C $min^{-1}$.

### 2.2. Preparation of $TiO_2$/N-OPK hybrid photocatalyst composites

Initially, 2 g N-OPK1, N-OPK2, or N-OPK3 were separately dispersed in 30 mL of ethanol in a 250 mL beaker and sonicated for 15 min. The dispersion was transferred to a magnetic stirrer, and 5 mL of TTIP were added, followed by vigorous stirring for 1 hour at room temperature. Subsequently, 70 mL of deionized water were slowly added with continuous agitation over another hour. The resulting slurry was allowed to age overnight, dried in an oven at 80 °C, and then calcined in air at 500 °C for 1 h using a heating ramp of 10 °C $min^{-1}$. After cooling to room temperature, the powders were washed neutral with DI water, dried, and stored for future use. The products are labelled T/N-OPK1, T/N-OPK2, T/N-OPK3 and OPKT with the letter T indicating the presence of titania in the materials. A pure $TiO_2$ (P-$TiO_2$) powder (control sample) was synthesized using the same procedure, excluding every other component but TTIP.

### 2.3. Photocatalyst characterization

Powder X-ray diffraction (PXRD) was done on a PANalytical Empyrean powder X-ray diffractometer (Malvern, U.K.) in a Bragg–Brentano geometry equipped with a PIXcel1D detector using Cu Kα radiation ($\lambda$ = 1.5419 Å) operating at 40 kV and 40 mA; $\theta/\theta$ scans were run from 4 to 70° 2$\theta$ with a step size of 0.0131° and a sample rotation time of 1 s.

Scanning electron microscopy (SEM) and energy dispersive X-ray spectroscopy (EDXS) were done on a JEOL JSM-6510 (Freising, Germany) with a W filament operated at 15 kV and equipped with an Oxford Instrument Xplore EDXS detector. Small amounts of the samples were deposited on a carbon glue pad. Prior to analysis, all samples were sputtered under vacuum with Au/Pd using a Polaron Mini Sputter Coater SC7620. The back scattered electron (BSE) detector was used for material contrast, the secondary electron (SE) detector for topographic images at 15 kV.

Elemental analysis (CHNS) was done on an Elementar Vario EL III (Langenselbold, Germany) in duplicate. The limit of detection is 0.1 μg (N) and 0.5 μg (CHS) with an accuracy of 0.5%.

Attenuated total reflectance Fourier transform infrared (ATR-FTIR) spectroscopy was done on a Nicolet iS5 (Thermo Scientific, Waltham, MA, iD7 ATR unit with a diamond crystal, resolution of 4 $cm^{-1}$, 32 scans, from 400 to 4000 $cm^{-1}$).

Nitrogen sorption measurements were done on a Microtrac Belsorp MAX (formerly BEL instruments) and Microtrac Belsorp MINI X. Samples were prepared and activated in a Microtrac BELPREP VAC III vacuum degasser for 3 hours at 300 °C under dynamic vacuum prior to the nitrogen sorption measurements to remove adsorbed gases and moisture. Specific surface areas (SSAs) were calculated using the Brunauer–Emmett–Teller (BET) model. Average pore sizes were estimated from the adsorption branch of the isotherm using the Barrett–Joyner–Halenda (BJH) method. The pore volume was determined at $P/P_0 > 0.99$.

Thermogravimetric analysis (TGA) was done on a Mettler Toledo TGA/DSC 3+ (Selb, Germany) from 25 to 1000 °C in air with a heating rate of 10 °C $min^{-1}$.

UV-visible diffuse reflectance measurements were done on a PerkinElmer Lambda 950 with a Praying Mantis™ attachment (Harrick Scientific Products Inc.). $MgSO_4$ Analar NORMAPUR (VWR) was used as a background material. Band gap energies of T/N-OPK1, T/N-OPK2, T/N-OPK3 and OPKT were estimated using Tauc's equation (eqn (1)):

$$(\alpha h\nu)^2 = A(h\nu - E_g) \quad (1)$$

where $\alpha$, $h\nu$, $A$, and $E_g$ are the absorption coefficient, photon energy, a constant, and band gap energy, respectively. $E_g$ was obtained using the baseline method.[45]

Photoluminescence (PL) spectra were recorded on a home-built micro-spectrometer. In short, a 355 nm (Coherent Genesis) laser was directed to the sample through a 40× objective (Nikon Plan Fluor ELWD). The excitation power at the sample plane was 1.5 mW. The emission signal was collected through

the same objective and separated from the excitation beam by a dichroic mirror (Chroma *zt* 375 RCD). Finally, the spectra were recorded by an imaging spectrograph (Andor Kymera 328i, equipped with an Andor Newton EMCCD). The final spectra were averaged over 20 individual spectra each with an integration time of 1 s per spectrum.

X-ray photoelectron spectroscopy (XPS) data were obtained on an Axis Supra+ (Kratos Analytical, UK) using monochromatized Al $K_\alpha$ radiation for excitation (15 kV, typically 20 mA). CasaXPS software was used for data processing and interpretation. XPS signals were fitted using GL(30) line shapes, combining Gaussian (70%) and Lorentzian (30%) line shapes.

Total organic carbon (TOC) was measured on a Vario TOC analyzer (TOC/TNb Analyzer, vario TOC cube, Elementar Analysen systeme GmbH, Hanau, Germany).

Liquid chromatography-mass spectrometry (LC-MS) analysis was performed on an Agilent G6470A Series Triple Quad LC/MS (Agilent Technologies Sales & Services GmbH & Co.KG, Waldbronn, Germany) and HPLC Agilent Infinity 1260 System (binary pump, multicolumn thermostat, vial sampler VL, UV–vis Dual Wavelength Detector set at $\lambda_{TET}$ = 358 nm and $\lambda_{BPA}$ = 225 nm).

### 2.4. Evaluation of the photocatalytic activity

The photocatalytic activities of the composites were evaluated using a home-built photoreactor described previously[42] where four fluorescent lamps (Philips master PL-L 4p 36 W/840, 80 lm $W^{-1}$) provide the light source. The solution temperature was monitored throughout and remained around 28 °C during the entire experiment. The emission spectrum of the lamp can be found at (https://www.jllelectrical.com.my/showproducts/productid/4652965/cid/320296/philips-master-18w-pll-4pin-2g11-fluorescent-tube-3000k4000k6500k-927903008470/, Access date: December 5, 2025). The illuminance at the solution surface is 10 200 lux measured using a digital lux meter (LX1010BS, China). To precisely compare the rate constant $k$, the determination of the apparent quantum yield (AQY) would be necessary for the different materials. However, due to experimental limitations, these measurements were not possible with the current setup.

In each photodegradation experiment, 50 mg of either T/N-OPK1, T/N-OPK2, T/N-OPK3, or OPKT were dispersed in 100 mL of a 10 mg $L^{-1}$ aqueous BPA or TET solution. This mixture was stirred for 2 h under constant irradiation. Periodically, 2.0 mL aliquots were withdrawn and immediately filtered through a 0.45 μm PTFE syringe filter (VWR, Radnor, USA) into a brown HPLC vial for further analysis. To ascertain that the PTFE filters do not adsorb the contaminants and influence the measurements, untreated water samples containing the same contaminant concentration were also passed through the filter as a control. The residual concentration in the liquid phase was analysed using the Agilent G6470A Series Triple Quad LC/MS described above.

The degradation efficiency was determined using eqn (2):

$$R(\%) = \frac{C_0 - C_t}{C_0} \times 100 \quad (2)$$

where, $C_0$ and $C_t$ are the concentrations of the contaminant (mg $L^{-1}$) in the starting solution and after time $t$ of treatment with the photocatalyst composite, respectively.

The mineralisation efficiency was determined through the measurement of the TOC. The % mineralisation efficiency was calculated using eqn (3),

$$\%\text{Mineralisation} = \frac{TOC_0 - TOC_e}{TOC_0} \times 100 \quad (3)$$

where $TOC_0$ and $TOC_e$ refer to the TOC at the start of the experiment and the TOC after treatment, respectively.

The Langmuir–Hinshelwood (L–H) model was used to compare the degradation efficiency of all photocatalysts. The reaction rate is expressed as[46,47] (eqn (4))

$$r = -\frac{dC}{DT} = k\theta = \frac{kKC_0}{1 + KC_0} \quad (4)$$

where $\theta$ is the fraction of pollutant adsorbed at the interface, $k$ is the reaction rate constant, $K$ is the adsorption equilibrium coefficient and $C_0$ is the initial concentration of pollutants. When the pollutant concentration is low ($KC_0 \ll 1$), the reaction follows pseudo-first-order kinetics, and the integrated rate equation simplifies to eqn (5), with

$$\ln\frac{C_0}{C_t} = kt \quad (5)$$

Here, $C_0$ and $C_t$ (mg $L^{-1}$) are the initial pollutant concentration and concentration at time $t$, respectively. The variables $k$ ($min^{-1}$) and $t$ (min) denote the degradation rate constant and irradiation time, respectively; $k$ was determined from the slope of the linear regression data.

Furthermore, we explored the impact of operation variables on BPA and TET photodegradation using the photocatalyst composite with the highest catalytic performance, T/N-OPK3. To that end, the influence of photocatalyst dose was studied by agitating 100 mL of a 10 mg $L^{-1}$ contaminant solution (BPA or TET) while varying the photocatalyst dose from 10–100 mg.

The effect of the initial contaminant concentration on degradation was examined by mixing 100 mL of the contaminant solutions with contaminant concentrations between 5 and 40 mg $L^{-1}$ with 100 mg of the photocatalyst. For the assessment of the effect of pH, ionic strength, and anions, we used a contaminant solution with a fixed concentration of 10 mg $L^{-1}$ with a catalyst dose of 50 mg. The pH of each contaminant solution was adjusted between 3.0 and 11.0 using 0.1 M HCl or 0.1 M NaOH. Variations in ionic strength were achieved by comparing the effects of the photocatalyst *vs.* NaCl concentration (0.0, 0.01, 0.025, and 0.05 M). Likewise, the effect of different anions was studied using 1.0 mM solutions of $Na_2SO_4$, $NaHCO_3$, and $Na_3PO_4$.

To estimate the reusability of the composites, recycling experiments were carried out with the catalyst exhibiting the highest catalytic performance, T/N-OPK3. For every experiment, 100 mL of a 10 mg $L^{-1}$ BPA or TET solution were mixed with 200 mg of T/N-OPK3 and agitated at room temperature for 120 min under irradiation. The catalyst was filtered, washed

 

with water, dried at 80 °C, and used for the subsequent cycle under identical conditions as described above.

### 2.5. Analysis of the degradation products

Identification of the degradation products was done *via* high-performance liquid chromatography-mass spectrometry (HPLC-MS, Agilent Infinity HPLC 1260 System with an Agilent G6470A Series Triple Quad LC/MS, Agilent Technologies Sales & Services GmbH & Co.KG, Waldbronn, Germany) using solutions that were irradiated for 120 min in the presence of the photocatalyst. Separation was carried out using a Poroshell 120 EC-C18 column (3.0 × 50 mm, 2.7 µm; pressure limits 20–400 bar; temperature 25 °C, Agilent Technologies Sales & Services GmbH & Co.KG, Waldbronn, Germany). The sample injection volume was 10 µL at a flow rate of 0.6 mL $min^{-1}$.

For TET, the gradient mobile phase consisted of 0.1% formic acid (eluent A) and methanol (eluent B). The elution gradient for the mobile phase was: 0 min; 80% A, 0–3 min; 80–10% A, 3–5 min; 10% A, 5–5.01 min; 10–80% A, 5.01–7 min; 80% A.

For BPA, the mobile phase was 0.010 mol $L^{-1}$ ammonium formate (A) and methanol (B), with the following gradient: 0 min; 80% A, 0–3 min; 80–0% A, 3–5 min; 0% A, 5–5.01 min; 0–80% A, 5.01–6 min; 80% A. The difference to 100% is solvent B.

Analyses were performed in ESI positive ion mode using the following settings: nebulizer pressure of 35.0 psi, fragmentor voltage of 80 V, and a desolvation nitrogen gas at a flow rate of 11.0 L $min^{-1}$. MS scans were performed in the range = 100–1000 *m/z* at fragmentor voltage = 80 V with a scan time = 500 ms.[42]

### 2.6. Detection of reactive species

To understand the role of the key reactive species including holes $h^+$, hydroxyl radicals $^{\bullet}OH$, and superoxide radical anions $^{\bullet}O_2^-$ in the photodegradation, three scavengers, namely isopropanol (IPA), sodium oxalate ($NaO_x$), and benzoquinone (BQ), were introduced into the contaminant solutions to capture $^{\bullet}OH$, $h^+$, and $^{\bullet}O_2^-$, respectively.[42,48] In brief, 100 mg of the photocatalytic composite was dispersed in a 100 mL BPA or TET solution (10 mg $L^{-1}$) and then 1 mM sodium oxalate, 0.5 mM benzoquinone, or 0.2 mL isopropanol, respectively, were added to the mixture. This mixture was agitated for 120 min under irradiation, followed by HPLC and HPLC-MS as described in Section 2.5. Selection of scavenger concentration was based on previous reports.[30,49]

### 2.7. Removal of contaminants from an environmental sample

River water (2 L) was collected from the Nuthe River at the Nuthebrücke (Humboldtring) in Potsdam, Germany, using amber bottles for collection following the legal regulations of the State of Brandenburg on water collection from public surface waters (§25 Wasserhaushaltsgesetz). Initial physico-chemical properties such as pH (7.0) were measured directly after sample collection. Subsequently, the samples were stored at 4 °C until analysis. Before photocatalysis experiments, all samples were filtered through a 0.45 µm PTFE filter (ISOLAB, Germany) to eliminate suspended solids. In each experiment, 100 mL of filtered water were spiked with 10 mg $L^{-1}$of BPA or TET and mixed with 100 mg of the photocatalytic composite. The mixture was stirred and irradiated for 120 min, filtered and the filtrates were analysed as described above.

## 3. Results and discussion

### 3.1. Material characterization

Fig. 1 shows the FTIR spectra of the precursors and the composite materials. The spectra of kaolin, melamine, orange peel (OP), N-OPK1, N-OPK2, and N-OPK3 are shown in Fig. 1a. The kaolin clay exhibits weak bands between 1300–1500 $cm^{-1}$. These can be assigned to Si–O stretching and bending along with –OH bending vibrations. Notably, the broad band at 1039 $cm^{-1}$ stems from the Al–Si–O stretching vibration, and the band at 908 $cm^{-1}$ corresponds to Al–OH in-plane bending vibrations.[50] The doublet at 776 and 690 $cm^{-1}$ is due to Si–O–Si bridging bonds in quartz.[51,52]

The raw orange peel powder shows characteristic bands of lignocellulosic materials. The medium band between 3578 and

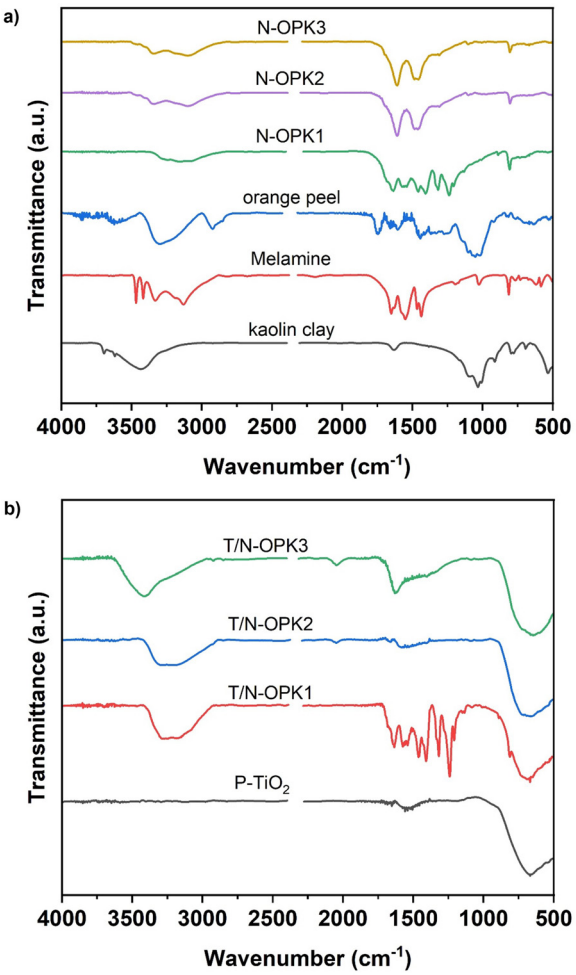


Fig. 1 (a) FT-IR spectra of kaolin clay, melamine, raw OP, N-OPK1, N-OPK2, and N-OPK3 composites and (b) FT-IR spectra of P-$TiO_2$, T/N-OPK1, T/N-OPK2 and T/N-OPK1 photocatalytic composites. The gap in the IR data is a cut for clarity – no signals have been observed in the cut region.

3027 $cm^{-1}$ stems from the –OH and –NH stretch vibrations of lignin. Additionally, the band at 2923 $cm^{-1}$ is assigned to the –C–H stretching vibration of methyl groups. Distinct bands corresponding to the C═O vibration of carboxylic acids or esters and aromatic C═C bonds are observed around 1746 and 1613 $cm^{-1}$, respectively.[31] The bands at 1103 and 1017 $cm^{-1}$ are due to C–O stretching vibrations of cellulose and hemicelluloses in lignocellulose.[53]

In the spectrum of melamine (Fig. 1a), bands at 3122–3500 $cm^{-1}$ are assigned to N–H stretching vibration modes, whereas the bands in the 1015–1640 $cm^{-1}$ range correspond to the C–N and C═N stretching vibrations of the heterocyclic frameworks in the 1,3,5-*s*-triazine ring.[54,55] Furthermore, the sharp band at ≈ 810 $cm^{-1}$ is characteristic of out-of-plane bending modes of the aromatic ring.[56] Bands between 457–770 $cm^{-1}$ are linked to the C–$NH_2$ group and its bending vibration modes.[7]

The nitrogen-doped hybrid clay composites N-OPK1, N-OPK2, and N-OPK3 display spectral patterns and characteristic bands similar to those of the precursors, but with a slight shift in position and intensity. Broad bands appearing at 3388 and 2933 $cm^{-1}$ correspond to N–H or O–H stretching vibrations. Typical features of melamine, including the out-of-plane $NH_2$ bending mode at 810 $cm^{-1}$ and the C–N and C═N stretching of the heterocyclic frameworks in the 1100–1700 $cm^{-1}$ range, are evident. Notably, numerous peaks are observed in the 1100–1700 $cm^{-1}$ range for N-OPK1, while two distinct peaks appear at 1610 and 1473 $cm^{-1}$ for N-OPK2 and N-OPK3. This variation is likely due to the presence of more organic residue in N-OPK1, which is not completely lost during calcination, compared to N-OPK2 and N-OPK3 which undergo longer calcination and correspondingly lose more of the organic components. This observation also suggests that structural transformation of the melamine monomer occurs upon increased thermal treatment, with possible formation of other melamine derivatives such as melem or melam.[57,58]

Fig. 1b represents the spectra obtained from the final $TiO_2$/nitrogen-doped hybrid clay photocatalyst composites. In the spectra of T/N-OPK1 and T/N-OPK2, a broad band around 3400–3000 $cm^{-1}$ is attributed to –$NH_x$ ($x$ = 1,2) from residual uncondensed amino groups in melamine and from O–H stretching vibrations.[58,59] For T/N-OPK3, this band is centered at 3419 $cm^{-1}$.

Furthermore, the bands in the range of 1000–1500 $cm^{-1}$, specifically at 1462 and 1082 $cm^{-1}$, correspond to Ti–N bond vibrations, suggesting N incorporation into the $TiO_2$ lattice.[60] These bands are more distinct in T/N-OPK1 but weakened in T/N-OPK2 and T/N-OPK3 as shown in the expanded spectra (Fig. S1, SI). This intensity loss is likely due to longer overall calcination times in the respective materials, which causes loss of organic components. Furthermore, a distinct band around 1629 $cm^{-1}$ in the spectra of T/N-OPK3 can be attributed to the stretching vibration of aromatic C–N heterocycles.[61] Finally, the intense peak observed around 600–700 $cm^{-1}$ can be assigned to a Ti–O stretching vibration, suggesting the presence of $TiO_2$ in the photocatalyst composites.[42]

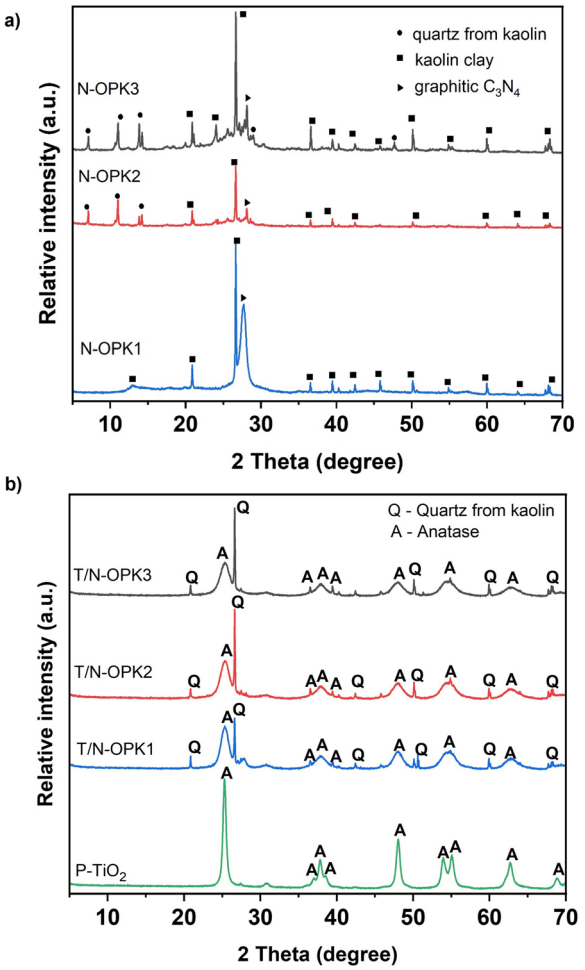


Fig. 2 XRD patterns of (a) N-doped hybrid clay composite and (b) the photocatalyst composites P-$TiO_2$, T/N-OPK1, T/N-OPK2 and T/N-OPK3.

The XRD patterns of the nitrogen-doped hybrid clay composites N-OPK1, N-OPK2, and N-OPK3 are shown in Fig. 2a. All patterns reveal characteristic reflections associated with quartz from the kaolin precursor.

Moreover, the diffraction pattern of N-OPK1 exhibits a broad reflection at 27.7°, corresponding to crystalline carbon nitride. This reflection disappearsin the XRD patterns of N-OPK2 and N-OPK3.[62,63]

Fig. 2b presents the XRD patterns obtained from $TiO_2$/nitrogen-doped hybrid clay photocatalyst composites, T/N-OPK1, T/N-OPK2, and T/N-OPK3. These patterns reveal the characteristic titania (101), (004), (200), (105), and (204) reflections indicative of the anatase phase of titania (ICSD 154603), with the main (101) reflection at 2$\theta$ of 25.4°. These reflections are broader than those observed for the control, P-$TiO_2$, suggesting the formation of nanocrystalline $TiO_2$ particles with smaller crystallite sizes in the modified photocatalyst composites.[64,65] The XRD patterns also confirm the presence of the kaolin clay starting material.

Elemental analysis (Table 1) also confirms the presence of nitrogen and carbon. These two elements may be present in

 

Table 1 Elemental analysis data and nitrogen sorption data (see discussion below) of the composites. Note that in these materials, there is also Al, Si, and O from the clay precursor, which cannot be detected using EA, but may slightly affect the precision of the EA measurement. $S_{BET}$ is the surface area determined from Brunauer–Emmett–Teller (BET) fitting. P-$TiO_2$ is a control sample (pure $TiO_2$ produced without any of the other components, see experimental section for details)

| | Material | | | | | | | |
|---|---|---|---|---|---|---|---|---|
| Property | N-OPK1 | N-OPK2 | N-OPK3 | T/N-OPK1 | T/N-OPK2 | T/N-OPK3 | OPKT | P-$TiO_2$ |
| C (at%) | 31.80 | 28.60 | 28.80 | 7.70 | 7.80 | 9.10 | 17.70 | 0.031 |
| N (at%) | 49.80 | 44.30 | 45.10 | 9.90 | 5.80 | 8.80 | 0.701 | 0.018 |
| $S_{BET}$ ($m^2$ $g^{-1}$) | 17.65 | 13.46 | 9.86 | 134.90 | 174.79 | 180.1 | 88.52 | 51.80 |
| Pore volume ($cm^3$ $g^{-1}$) | 0.1400 | 0.0975 | 0.0775 | 0.347 | 0.261 | 0.234 | 0.214 | 0.203 |
| Average pore diameter (nm) | — | — | — | 10.282 | 5.977 | 5.193 | — | — |

either the carbonaceous component of the composites (*i.e.* in the biochar, possibly N-doped biochar, and in the respective melamine components) and additionally, some fraction of C and N may also be present in the $TiO_2$ lattice as a dopant, consistent with literature.[66] Among others, literature suggests that coordination of nitrogen to titanium (*e.g.* ···N–Ti–N··· bonding patterns) may lead to peak broadening,[67] which is consistent with our observations in the XRD patterns.

Scanning electron microscopy (SEM) images of the materials are shown in Fig. 3. The morphology of the N-OPK materials is rather similar. All N-OPK materials consist of flaky and rather polydisperse particles. Longer calcination times may favour the formation of larger or a bit more densely stacked melamine crystalline regions, similar to literature,[68] but this is difficult to conclude from microscopy alone.

The T/N-OPK materials consist of the same flaky particles but the addition of the $TiO_2$ also produces a very large number of small, rather densely packed particles on the surface of the flaky support particles. Likely, these are $TiO_2$ particles deposited onto the existing flaky N-OPK substrate particles.

The energy dispersive X-ray (EDX) spectra collected from T/N-OPK3 indeed confirm the presence of Ti (indicating the presence of $TiO_2$) along with additional elements such as C, N, Al, and Si originating from the nitrogen-doped hybrid clay composites, Fig. 3. The O signal is caused by the presence of titania and clay, both of which contain O. The N signal likely

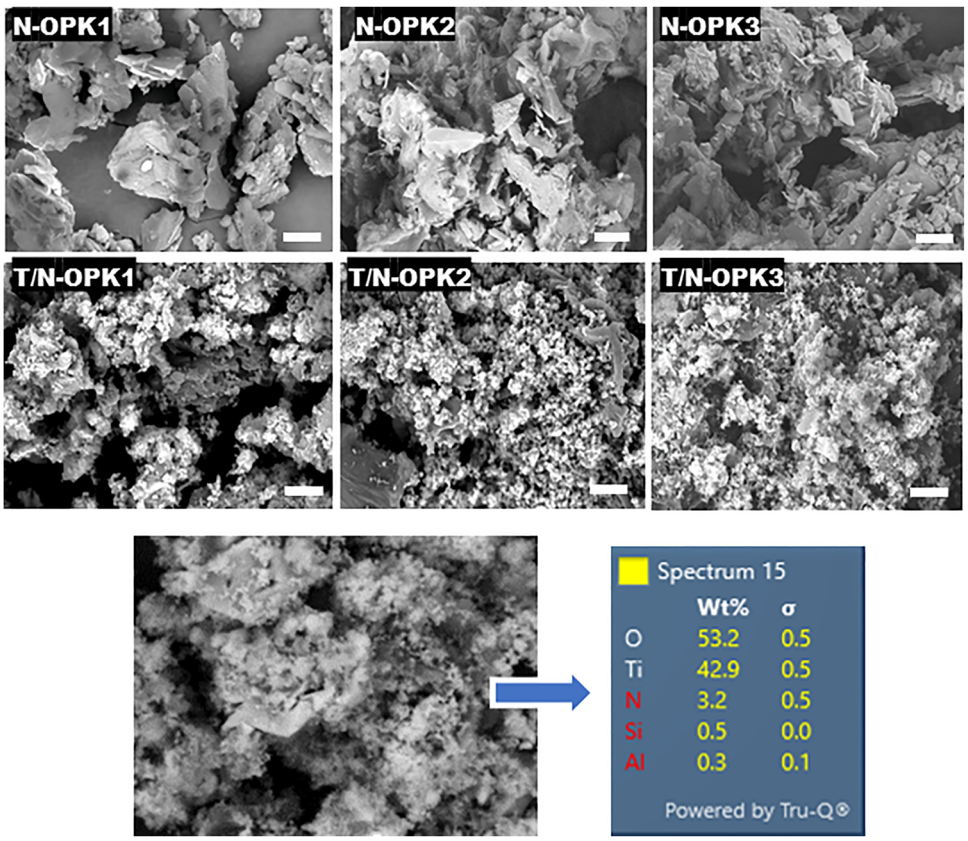


Fig. 3 SEM images of prepared materials and the EDX data set of T/N-OPK3. The scale bar is 10 μm in all images. Images of the pristine materials can be found in Fig. S2, SI.

stems from melamine (and melamine reaction products) and from OP residues present in the material. The C signal stems from the presence of the biochar along with melamine (and melamine reaction products). Al and Si signals stem from the clay components within the composites. Furthermore, elemental maps of the composites (Fig. 4) prove a uniform distribution of all elements within the composites.

As a result, EDX spectroscopy supports elemental analysis (EA, Table 1), which confirms the presence of C, H, and N in the composites. A slight, but not very clear, decrease in C and N content is observed across the precursor composites (without titania), which is likely due to the gradual loss of organic components during prolonged thermal treatment.

The photocatalyst composites T/N-OPK1, T/N-OPK2, and T/N-OPK3 generally contain a lower C and N fraction than the precursor composites N-OPK1, N-OPK2, and N-OPK3. The rather significant C and N reduction from the N-OPK materials to the T/N-OPK materials can be attributed to the higher thermal treatment temperature (500 °C) used in the second calcination step during $TiO_2$ incorporation. This likely promotes further thermal decomposition of some of the organic components present in the reaction mixture.[61] Furthermore, the photocatalyst composite without the melamine precursor, OPKT, contains the least amount of N, further confirming that melamine serves as the nitrogen source in the photocatalyst system.

The surface area and pore structure of the photocatalyst composites, along with the control composites were analysed using $N_2$ sorption, Fig. S3a. All photocatalyst composites (T/N-OPK1, T/N-OPK2, and T/N-OPK3) produce type IV isotherms with hysteresis loops and type III characteristics, indicating the presence of mesopores within the materials.[61,69] The specific surface area (SSA) and pore volumes obtained from the $N_2$ sorption analysis are presented in Table 1. Most importantly, Table 1 illustrates that the nitrogen-doped hybrid clay precursors N-OPK1, N-OPK2, and N-OPK3 exhibit low SSAs due to their low-temperature synthesis, where significant porosity does not develop. Prolonged heating (1–3 h) further reduces surface area through carbon residue deposition and minor structural collapse.[70,71]

In contrast, the photocatalyst composites display higher SSAs and total pore volumes, as the elevated temperature (500 °C) of the second calcination step promotes oxidative removal of residues, kaolinite dehydroxylation, and stabilization of additional porosity. This is advantageous, because at least in theory, higher surface areas and open porosities with relatively uniform $TiO_2$ particle distribution (see SEM images, Fig. 3) should provide a higher number of active sites.

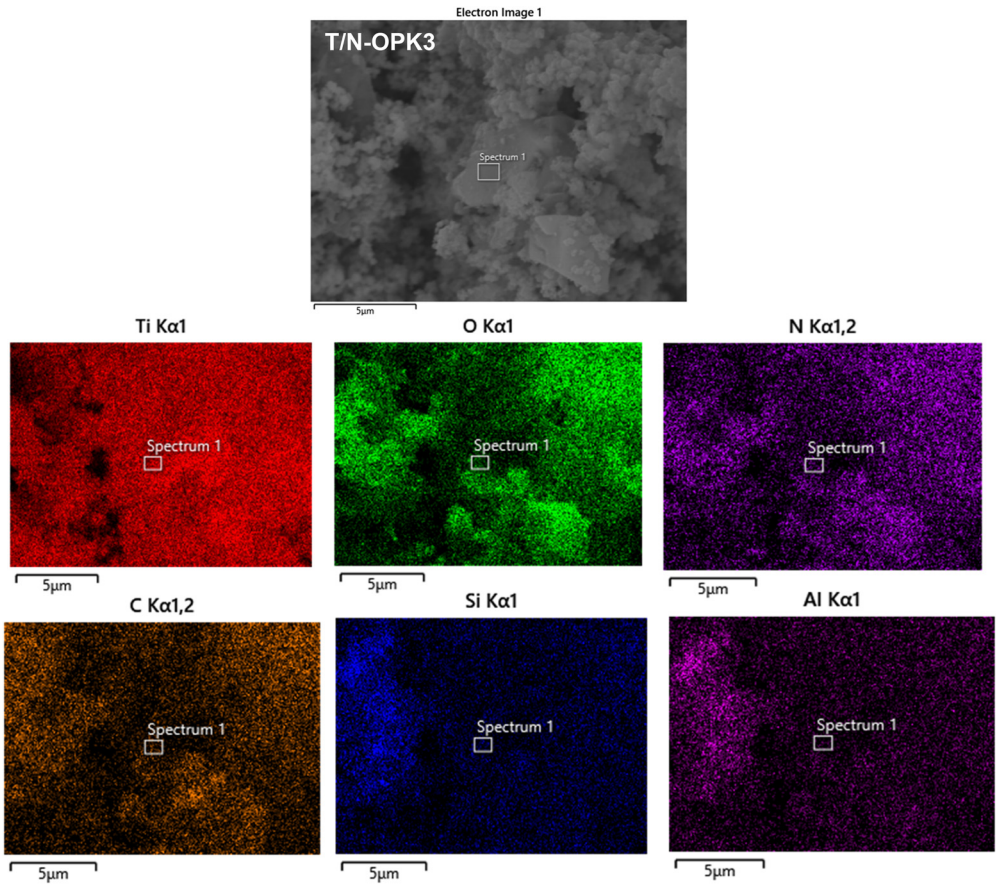


Fig. 4 Elemental distribution of the elements present in T/N-OPK3. The frame 'spectrum 1' represents the location where the initial EDX spectrum was recorded to identify the elements that needed mapping.

 

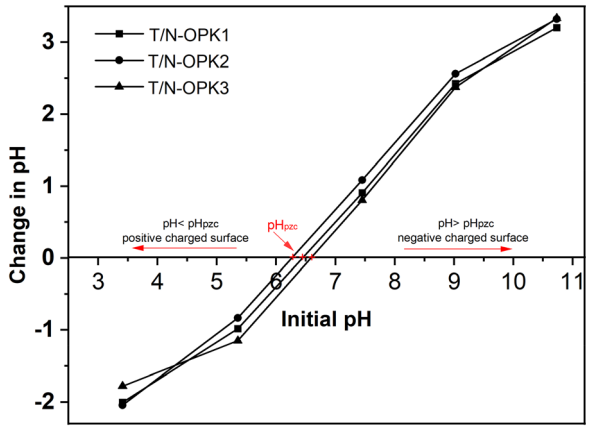


Fig. 5 $pH_{pzc}$ plots for the photocatalyst composites.

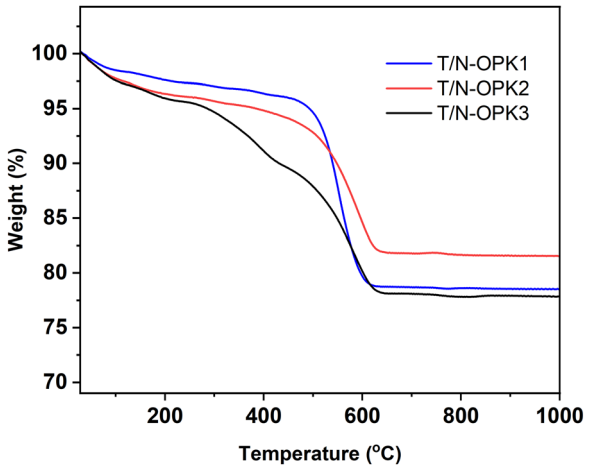


Fig. 6 TGA data obtained from the T/N-OPK1, T/N-OPK2, and T/N-OPK3. TGA was done in air.

This should promote the contact between the reactive oxygen species and contaminants,[72] which in turn should lead to an enhanced catalytic efficiency.

Barrett–Joyner–Halenda (BJH) analysis (Fig. S3b, SI) of the pore sizes and pore sizes distribution finds average pore diameters in the range of 5–10 nm, that is, the materials are mesoporous.[73] This should further enhance pollutant adsorption.

The point of zero charge ($pH_{pzc}$)[31] is a critical parameter for assessing the net surface charge and the pH at which particles become electrically neutral.[74,75] For T/N-OPK1, T/N-OPK2, and T/N-OPK3, $pH_{pzc}$ values are 6.44, 6.27, and 6.66, respectively (Fig. 5). These results align with previous studies, which report the isoelectric point of $TiO_2$ nanoparticles within pH 6.0–6.5.[76,77] Below the $pH_{pzc}$, the composite particles exhibit a positive surface charge. Above the $pH_{pzc}$, they are negatively charged.

Thermogravimetric analysis (TGA) of the photocatalyst composites, Fig. 6, illustrates the weight loss of the materials in air from 25 to 1000 °C. All composites exhibit a total weight loss of approximately 19 to 22%, but the individual steps are broad and difficult to separate clearly.

Initially, all photocatalysts show a rather rapid weight loss from room temperature to *ca.* 110 °C of about 5%. This weight loss can be assigned to water loss and removal of further volatile substances on the surface of the materials.

Following this first desorption step, T/N-OPK1 and T/N-OPK2 show a long and rather nondescript, continuous weight loss between *ca.* 150 and *ca.* 450 °C, followed by a more pronounced further weight loss between *ca.* 460 and 630 °C. The former process is likely associated with the decomposition of carbonaceous species from the biomass precursor.[78]

The latter, final weight loss is assigned to a mixture of processes including further decomposition of organic matter (orange peel, melamine, possibly melem or melam), further melamine condensation, along with silanol condensation and concurrent water release from the clay component. T/N-OPK3 in principle shows the same behaviour, but the second decomposition process between between *ca.* 150 and *ca.* 450 °C is a bit more resolved, indicating a slightly more distinct series of thermal decomposition steps.

T/N-OPK3 and T/N-OPK1 lose 8–10% more weight than T/N-OPK2 at high temperatures than T/N-OPK2. This difference may be attributed to variations in the carbon and nitrogen content, which undergo oxidation in air,[79] but this may also be due to some variability in the materials. The EA data, Table 1, do indeed confirm that there is some difference in the carbon and nitrogen content between these materials, although there is no clear trend.

UV–Vis diffuse reflectance spectroscopy (UV-DRS) was performed to determine the optical properties of the materials, Fig. 7a. The spectra reveal that the unmodified $TiO_2$ (P-$TiO_2$) has an absorption edge at around 402 nm, which is characteristic of anatase $TiO_2$.[80,81] In contrast to P-$TiO_2$, all photocatalyst composites show significant optical absorption in the visible region between 400–600 nm.

The optical band gaps ($E_g$) of the materials obtained from the Tauc plots (Fig. S4) are 3.27, 3.24, and 3.11 eV for T/N-OPK1, T/N-OPK2, and T/N-OPK3, respectively. These band gaps are significantly lower than $E_g$ obtained for the pure titania control sample P-$TiO_2$ at 3.30 eV. Possibly this reduction in $E_g$ is caused by the incorporation of impurities into the $TiO_2$ lattice from the precursors (biomass, melamine, clay). These impurities may create new energy levels within the $TiO_2$ band gap leading to a reduction in the overall band gap.[36,60]

Photoluminescence (PL) measurements (Fig. 7b) show that the photocatalysts display stronger PL emission than the controls. This can be attributed to the creation of new emissive states and enhanced light absorption promoted by N-modification.[82] While PL intensity often reflects recombination rates, photocatalytic activity is also influenced by charge separation at heterojunction interfaces and better light utilization, explaining the higher activity observed in the composites (see below).[83] P-$TiO_2$ show the lowest emission, which appears masked in the stacked spectra due to the dominant PL peak of T/N-OPK1.

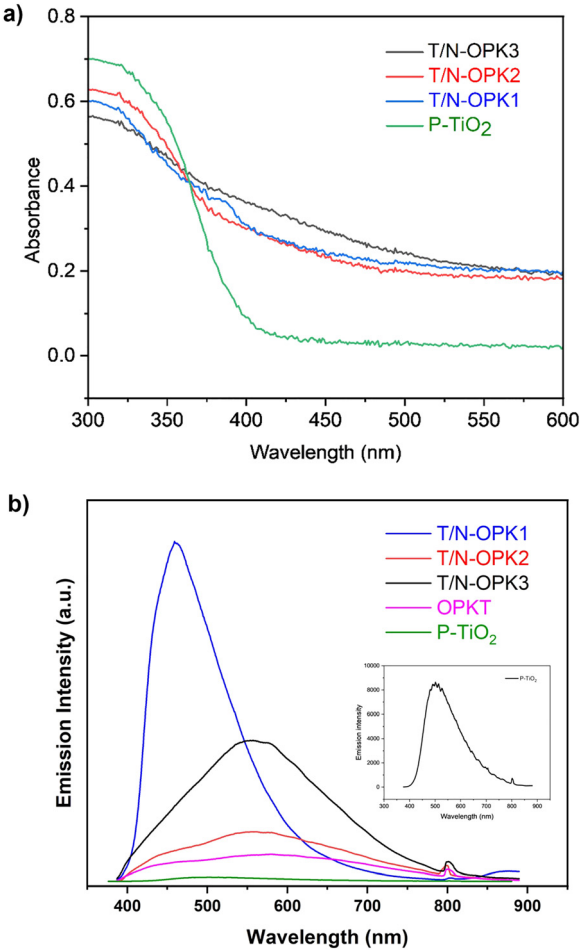


Fig. 7 (a) UV–vis DRS data, (b) PL spectra of OPKT, T/N-OPK1, T/N-OPK2, and T/N-OPK3. Inset in panel (b) is a magnified view of the PL spectrum of P-$TiO_2$.

In addition, the composites exhibit a noticeable red shift in their PL emission bands. This shift is generally due to bandgap narrowing and presence of defect states, which extend light absorption into the visible region, facilitate interfacial charge transfer, suppress electron–hole recombination, and enhance photocatalytic performance.[84,85] T/N-OPK1 exhibits the highest PL peak intensity, with a broad emission band centered at 457 nm. By contrast, T/N-OPK2 and T/N-OPK3 show lower PL peak intensities with broad emission bands centered at around 567 nm. Such emission bands observed between 449 and 570 nm are often associated with shallow traps linked to surface oxygen vacancies and lattice defects in$TiO_2$.[30,78,86] The reduced PL intensity of T/N-OPK2 and T/N-OPK3 indicate a reduced recombination rate of these electron–hole pairs *vs.* the recombination rate in T/N-OPK1.[87]

XPS analysis was conducted to investigate the elemental composition and chemical state of the elements in T/N-OPK3 and OPKT (that is, the melamine-free control material), respectively. Fig. 8a shows the survey spectra of T/N-OPK3 and OPKT from 0 to 1200 eV, where the N 1s signal of T/N-OPK3 shows a fairly strong intensity due to the presence of melamine during the synthesis as compared to that of OPKT. At the same time, the Si 2p and Al 2p signals have a lower intensity in the spectra of T/N-OPK3 than in the spectra of OPKT without melamine (details in Fig. S5, SI).

In Fig. 8b, the binding energies of the C–C bonds in the spectra of both materials were charge-corrected by setting it as equal at 284.8 eV, and the oxygen-bound species of C 1s were fitted as C–O, C═O, and O–C═O bonds at 286.2, 287.8, and 288.8 eV equally in both samples, respectively.[88,89] In addition, spectra of both materials show the binding energy of an Al–C–O bonding situation at 283.56 eV,[90,91] which implies that various functional groups, *e.g.* alcohol and carbonyl groups stemming from OP, can form bonds with elements stemming from the kaolin at the relatively high calcination temperature of 500 °C.[42,92]

In this research, the manipulated variable between both samples is the melamine applied during the reaction. Considering the possibility that melamine can undergo chemical transformation at 500 °C, one can infer three kinds of possible reactions:

(1) no reaction (*i.e.*, keeping the chemical structure of melamine intact),

(2) the formation of melam or melem *via* thermal condensation (Scheme S1 and Fig. S6), and

(3) the cleavage of C═N–C or/and terminal –$NH_2$ bonds by thermal decomposition.[93]

For a definite validation of the chemical changes and structures of melamine products during the reaction, the thermal condensation reaction of melamine was independently performed at 300 and 500 °C as monitored by XPS analysis (Fig. S3). The resulting XPS data show that the three N-coordinated carbon ($C_{3N}$) and terminal –$NH_2$ peaks shift to 287.99 eV (C 1s) and 400.94 eV (N 1s) after the reaction at 500 °C. This is consistent with literature[93] and indicates that in this study only pure melamine (control) undergoes thermal condensation to form melem.

However, Fig. 8c shows that the binding energies of the terminal –$NH_2$ (399.44 eV) and C═N–C (398.36 eV) in T/N-OPK3 do not undergo a massive positive peak shift toward higher binding energy when compared to those of melamine, which shows signals at 399.20 and 398.32 eV, respectively. This differs from the binding energies of the terminal –$NH_2$ and C═N–C in melam or melem (Fig. S6). Even the slightly shifted terminal –$NH_2$ component towards higher binding energy probably alludes to the existence of interstitial nitrogen species bound to hydrogen.[94,95] This suggests that melem or melam is not present in the photocatalyst composites.

In N-doped $TiO_2$, the N 1s signals at 400–403 eV can be assigned to oxynitride doping species such as Ti–N–O and Ti–O–N.[96,97] The slightly shifted $N^+$ resonance peak at 400.61 eV, accompanied by peak broadening, in the T/N-OPK3 sample further supports the presence of oxynitride doping.

Furthermore, Fig. 8b shows that the $C_{3N}$ peak of T/N-OPK3 is located at 287.68 eV which is a lower binding energy than that of melamine at 287.93 eV (Fig. S6). In principle, in the binding energy shifts that can be observed in XPS spectra, the more chemical bonds with electronegative atoms are present in a

 

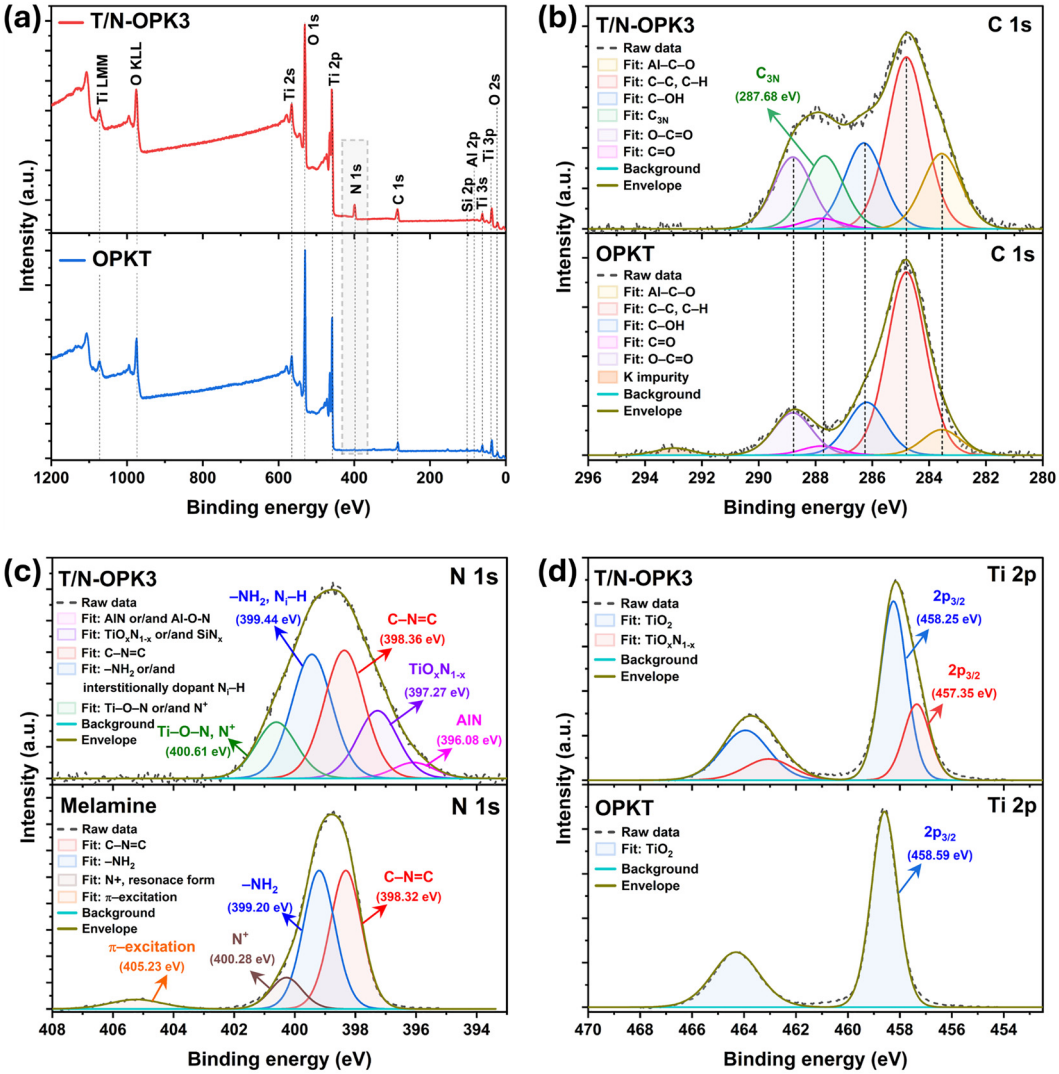


Fig. 8 High-resolution XPS spectra of T/N-OPK3 and OPKT, respectively. (a) Survey spectrum, (b) C 1s region, (c) N 1s region including N 1s of melamine, and (d) Ti 2p region. The quantitative results of the XPS measurements and the XPS fitting parameter of the C 1s, N 1s, Ti 2p are shown in Tables S1–S4 (SI).

chemical structure, the larger the positive XPS chemical shift.[98,99] Thus, this negative XPS chemical shift indirectly implies the possibility of the N–C=N bond cleavage (*i.e.*, chemical bonds in the $C_{3N}$ peak) during the reaction.

Considering all this, the XPS data suggest that melamine may undergo a thermal decomposition at 500 °C and does not react *via* the more common thermal condensation reaction toward melem or melam.[93,100] In particular, the spectrum of T/N-OPK3 shows two more peaks at 397.27 and 396.08 eV, which can be assigned to titanium oxynitride ($TiO_xN_{1-x}$)[101,102] or $SiN_x$,[103] and AlN.[104] Also, the lower XPS chemical shift of the Al 2p and Si 2p signals in T/N-OPK3 compared to those of OPKT supports the notion of an N-incorporation not only into the $TiO_2$ but also into the chemical structure of the kaolin clay (Fig. S5).

Fig. 8d shows photoelectron signals from Ti 2p in OPKT and T/N-OPK3, which are composed of doublet peaks with a 2 : 1 intensity ratio due to their degeneracies. The Ti $2p_{3/2}$ and Ti $2p_{1/2}$ peaks for OPKT are located at 458.59 and 464.31 eV with a doublet separation of 5.72 eV, respectively. This typically indicates a $Ti^{4+}$ species in anatase $TiO_2$.[105] On the contrary, the Ti 2p peak of T/N-OPK3 requires two components at 458.25 and 457.35 eV in Ti $2p_{3/2}$, respectively. The first component can be assigned to the $Ti^{4+}$–O (Ti $2p_{3/2}$) bond, which is shifted towards lower binding energy from 458.59 to 458.25 eV compared to OPKT. This observation can likely be attributed to some N-incorporation into the $Ti^{4+}$–O lattice. Another possible cause for this effect could be strong interactions between the anatase $TiO_2$ and the N-modified kaolinite with Al–N, Al–O–N, or Si–N bonds.[101] Also, the second component at 457.35 eV of T/N-OPK3 can be assigned to $Ti^{3+}$in Ti–N and/or N–Ti–O bonds in $TiO_xN_{1-x}$.[101,102]

In addition, this data strongly supports the assignment of the 397.27 eV signal to $TiO_xN_{1-x}$ (Fig. 8c). The presence of

$TiO_xN_{1-x}$ components in the N 1s and Ti 2p XPS signals of T/N-OPK3 further suggests that, during the synthesis of the photocatalyst composites, the melamine precursors are mainly consumed as a nitrogen source rather than undergoing a thermal condensation reaction to form a heptazine-based melem structure.

### 3.2. Photocatalytic activity of the composites

The photocatalytic degradation of BPA and TET was investigated in the presence of T/N-OPK1, T/N-OPK2, and T/N-OPK3 as well as in the presence of P-$TiO_2$ and OPKT (*i.e.* pure $TiO_2$ and a melamine-free composite, respectively) as controls under visible light irradiation, Fig. 9a and b. Further control experiments were done in the absence of any catalyst to evaluate the BPA and TET degradation *via* direct photolysis (*i.e.* direct photodegradation-by-irradiation) only.

In the case of BPA (Fig. 9a), there is no degradation in the absence of a catalyst, proving that the contribution of photolysis to BPA degradation is negligible. Once a catalyst is added to the mixture, BPA is degraded rather effectively. The order of photocatalytic activity is T/N-OPK3 (82% BPA degradation in 120 min) > T/N-OPK2 (75%) > T/N-OPK1 (52%) > OPKT (16%) > P-$TiO_2$ (around 0%). For TET degradation all photocatalysts show excellent activity, Fig. 9b. The degradation rate is very high and within 30 min, about 99% degradation is achieved with all catalysts. The order of the degradation rate is T/N-OPK2 > T/N-OPK1 > T/N-OPK3/T > OPKT > P-$TiO_2$ > Photolysis.

Degradation kinetics were analysed using the simplified pseudo-first order Langmuir–Hinshelwood kinetic model (eqn (5)) to determine the apparent rate constant $k$. The corresponding plots and values are presented in Fig. 9c, d and Table S1. For BPA (Fig. 9c), the normalized rate constants $k$ by catalyst mass are 0.119, 0.200, and 0.256 $min^{-1}$ $g^{-1}$, respectively, for T/N-OPK1, T/N-OPK2, and T/N-OPK3. Taking the highest $k$ and lowest $t_{1/2}$ as indicators for the most effective catalyst,[87] T/N-OPK3 ($k$ = 0.256 $min^{-1}$ $g^{-1}$, $t_{1/2}$ = 54 min) is the most effective photocatalyst for BPA degradation.

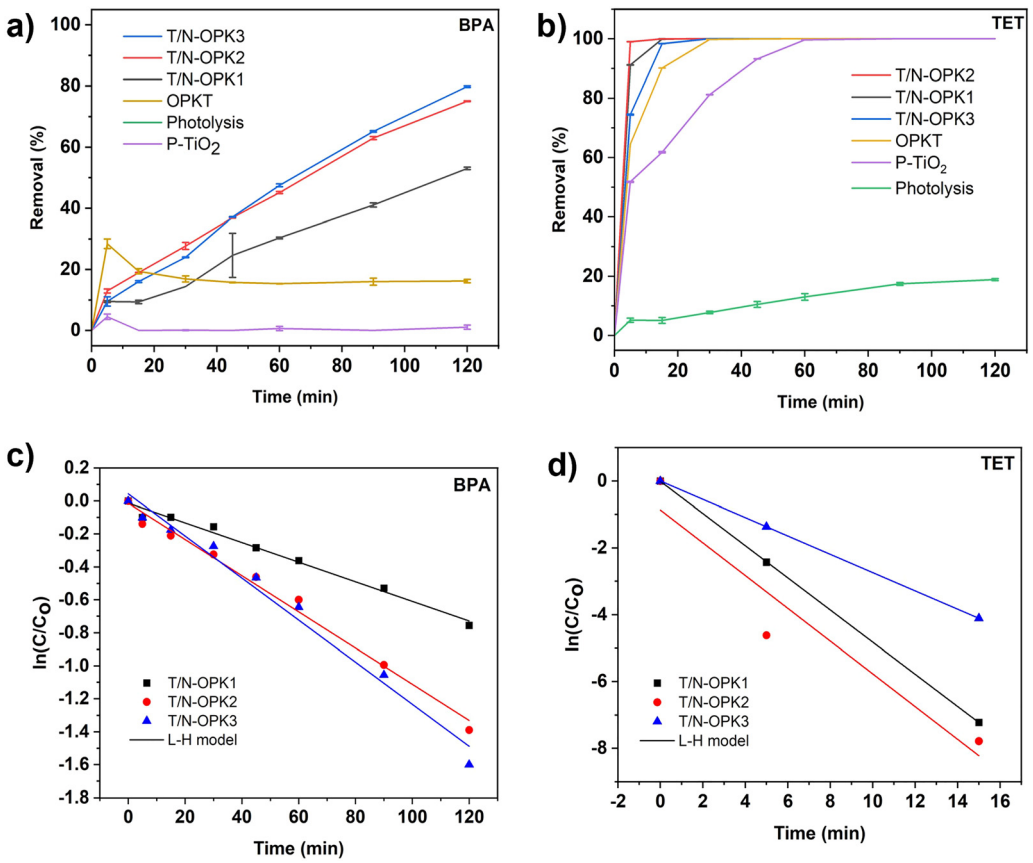


Fig. 9 (a) Degradation (% removal) of BPA under visible light *vs.* exposure time, (b) Langmuir–Hinshelwood kinetic model for BPA degradation, (c) degradation (% removal) of TET *vs.* exposure time and (d) Langmuir–Hinshelwood kinetic model for TET degradation *vs.* different catalysts and catalyst-free experiment (photolysis). Note that most error bars in panels (a) and (b) are small and therefore not visible in this graph. To evaluate if there is a direct correlation between surface area and rate constant $k$, we have also plotted the rate constant *vs.* total surface area of the 50 mg of catalyst in the experiment. However, these data only show a weak influence of the surface area on the rate constant, see Fig. S6, SI. In the case of TET, the data suggests a small reduction in k with an increase in surface area. In contrast the data suggests a small increase in k with increasing surface area for BPA. All linear fits exhibit correlation coefficients ($R^2$) close to 1, indicating a good fit with the kinetic model. Comment: Another option to study contaminant adsorption/photodegradation is the pre-adsorption of the contaminants in the dark for an extended period of time, followed by irradiation and concurrent photodegradation. However, we have decided to not study this process because it is less practical from an application point of view.

 

For TET (Fig. 9d), the respective normalized rate constants determined for T/N-OPK1, T/N-OPK2 and T/N-OPK3 are 9.62, 9.82, and 5.48 $min^{-1}$ $g^{-1}$. The photocatalyst with the best performance is T/N-OPK2, which has the highest $k$ (9.82 $min^{-1}$ $g^{-1}$) and the lowest $t_{1/2}$ (1.41 min). Table S5 (SI) summarizes the rate constants and half-lifes ($t_{1/2}$) of each photocatalytic composite for both the degradation of BPA and TET, respectively.

Dark studies conducted under the same experimental condition (but without visible light irradiation) show that the removal of BPA *via* simple adsorption on the photocatalyst surface is below 7%, Fig. 10a. This indicates that adsorption plays a minimal role in BPA removal and that BPA is only effectively removed in the presence of the photocatalysts.

In contrast, approximately 64%, 62%, and 58% of TET are removed by adsorption using T/N-OPK1, T/N-OPK2, and T/N-OPK3, respectively, Fig. 10b. This suggests that the surface of the photocatalyst has a higher affinity for TET than BPA. The degradation efficiency of the materials suggests that their strong adsorption affinity for TET is advantageous for photodegradation, as it allows more TET molecules to concentrate around the loaded $TiO_2$, thereby enhancing the rate of photooxidation. The equilibrium adsorption capacities ($q_e$) of BPA and TET on the T/N-OPK catalysts under dark conditions are presented in Table S5 (SI).

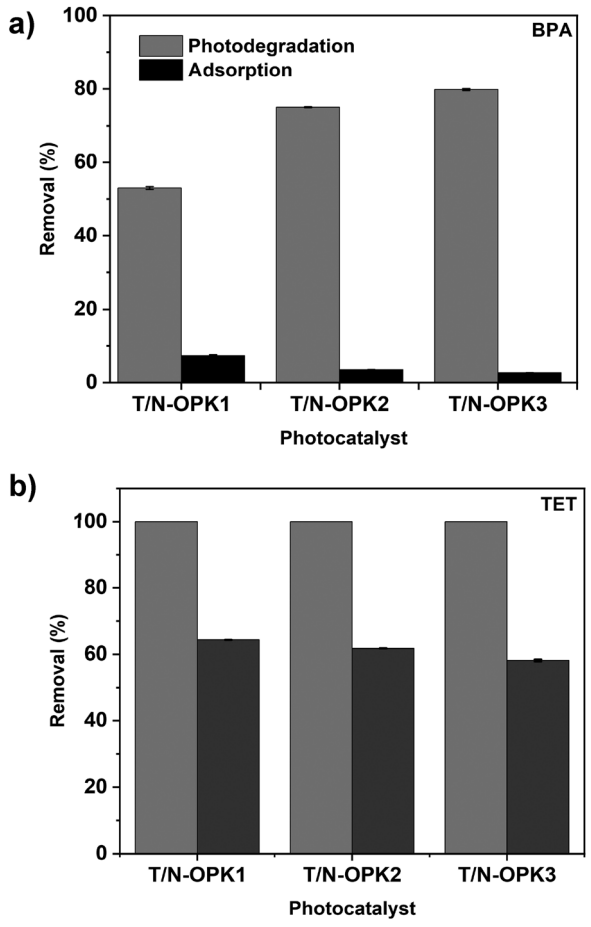


Fig. 10 Comparison of adsorption and photodegradation of (a) BPA and (b) TET *vs.* photocatalyst. Note that the errors bars in the data for TET are exceptionally small; this indicates an unusually high reproducibility of the experiments.

Overall, the T/N-OPK composites exhibit remarkable photocatalytic efficiencies for BPA and TET degradation to those of the control materials (P-$TiO_2$ and OPKT). In contrast, photolysis shows only minimal activity, confirming that the contaminants do not readily undergo self-degradation upon irradiation. The catalyst performance also far exceeds the efficiencies of our previous photocatalyst prepared without melamine.[42]

It must be stressed here that there may be two effects contributing to this advantageous behaviour: (1) the change of the optical properties and (2) different SSAs upon incorporation of melamine into the system. OPKT (which contains no melamine) has a comparatively low SSA of 88.52 $m^2$ $g^{-1}$ while the SSAs of the composite materials increase to *ca.*135–180 $m^2$ $g^{-1}$. In addition, the introduction of nitrogen appears to alter the $TiO_2$ band structure, as evidenced by lower band gaps (Fig. 7a and Fig. S4) and a visible red-shift in the absorption edge of the composites (Fig. 7).[106]

Therefore, we attribute the improved photoactivity of the T/N-OPK composites to the synergistic effects of enhanced visible light absorption and increased accessibility of active sites on well-dispersed doped $TiO_2$ particles on the surface of the composite catalysts.

### 3.3. Effect of operating parameters on degradation

Finally, a series of operating parameters on BPA and TET removal were studied. The solution pH plays an important role in the adsorption and photodegradation of organic molecules by influencing the surface charge of the photocatalysts and the charge of organic molecules in solution. This will in turn directly affect how well a photocatalyst and a contaminant interact.[107] In this study, the effect of the initial solution pH (3.0–11.0) on BPA and TET photodegradation was investigated using the best performing composite, T/N-OPK3. Given that the $pH_{pzc}$ of T/N-OPK3 is at pH 6.6, the surface of T/OPNK3 is positively charged at pH $<$ pH 6.6 and negatively charged when pH $>$ pH 6.6.

Fig. 11a shows that the photodegradation of BPA is most efficient at neutral pH, following the sequence: pH 7.0 $>$ pH 5.0 $\approx$ pH 9.0 $>$ pH 3.0 $>$ pH 11.0, similar to data by Wang and Lim.[108] The lowest rates of BPA degradation are observed at strongly acidic (pH 3.0) and strongly basic (pH 11.0) conditions. As BPA has a $pK_a$ $\sim$9.6, it is positively charged at pH $<$ 9.6 and negatively charged at pH $>$ 9.6.[109] Therefore, under highly acidic conditions, both the surface of the catalyst and the BPA molecules are positively charged, which likely results in a net electrostatic repulsion between adsorbent and adsorbate and thereby hampers the photocatalytic BPA degradation. Similarly, at very basic conditions, both the catalyst surface and the BPA molecule are negatively charged. This again likely results in electrostatic repulsion between adsorbent and adsorbate.

As a result, the optimum pH for BPA photodegradation is around pH 7. Around pH 7, the catalyst surface is negatively

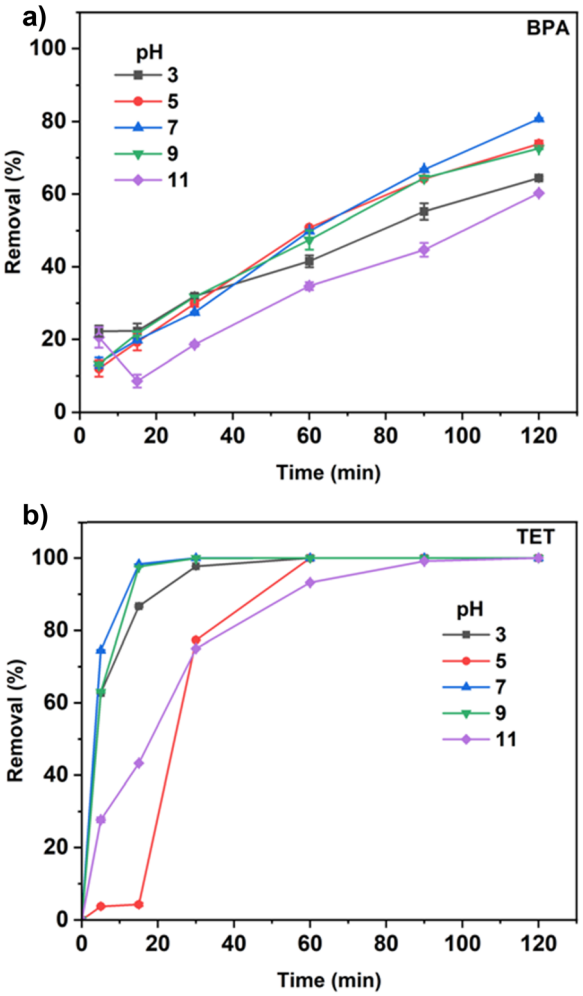


Fig. 11 Effect of solution pH on (a) BPA degradation and (b) TET degradation with T/N-OPK3.

charged while BPA is positively charged resulting in a net attraction, which enhances the effective contact between contaminant and photocatalyst and results in the most effective BPA degradation.

For TET, Fig. 11b, the degradation rates follow the order: pH 7.0 ≈ pH 9.0 > pH 3.0 > pH 5.0 > pH 11.0. At pH 7.0 and 9.0, *ca.* 100% removal efficiency is achieved within 10 min, indicating a very fast degradation, whereas at pH 11.0 the same efficiency is only reached at 90 min. This can again most simply be explained by TET speciation ($pK_a \approx 7.68$) and the surface charge of T/N-OPK3 ($pH_{pzc} = 6.6$). Around neutral pH, TET is in its zwitterionic form, while the catalyst surface is near its isoelectric point. This minimizes electrostatic repulsion, promotes favourable adsorption and surface complexation, and accelerates degradation. Possibly, there are further interactions like van der Waals forces, π–π stacking between TET and graphitic structures in the biochar components, or hydrogen bonding interactions as well that contribute to a strong adsorption of TET to the photocatalyst surface as shown in Fig. 10b above.

At strongly basic pH (pH = 11.0), TET predominantly exist as anionic species, while the catalyst surface is also negatively charged. This again results in strong electrostatic repulsion which reduces adsorption and consequently reduces the degradation rate.[110,111]

Fig. 12a shows that the photodegradation rate of BPA decreases with increasing initial BPA concentration. The degradation efficiency of BPA reaches 99.9% at a low BPA concentration of 2 mg $L^{-1}$ after 120 min. However, at a higher BPA concentration of 20 mg $L^{-1}$, the degradation efficiency decreases to about 60% after 120 min.

We currently hypothesize that the active sites on the T/N-OPK3 surface may be covered with BPA molecules at high initial concentrations. This would lead to (1) a reduced accessibility of the active sites for BPA and (2) possibly also to a reduced light absorption by the photocatalyst. The latter could then reduce the number of reactive oxygen species (ROS) that are generated on the photocatalyst surface and hence lead to a reduced BPA

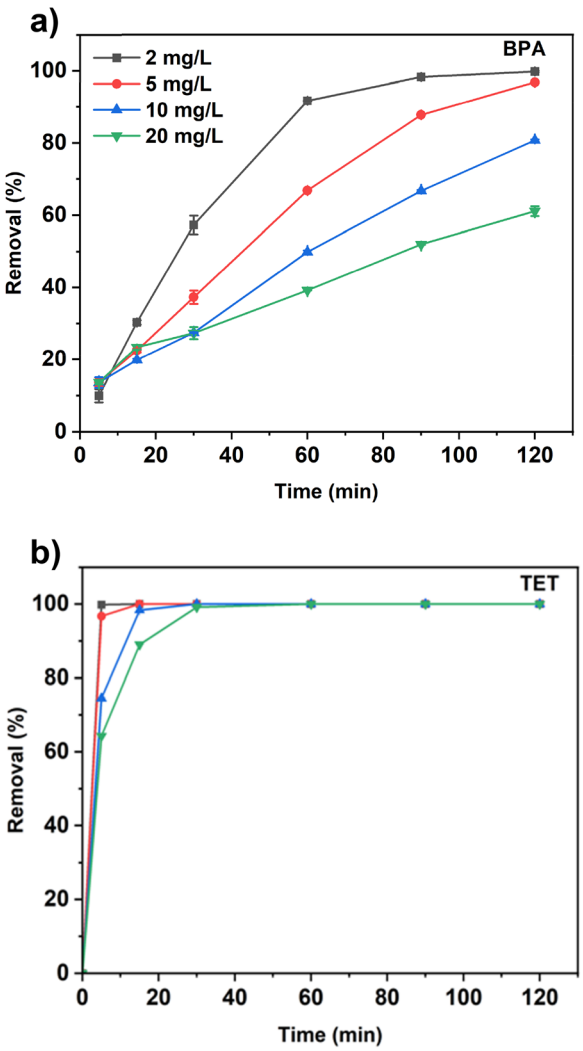


Fig. 12 Effect of initial concentration on the degradation of (a) BPA and (b) TET *vs.* time using the T/N-OPK3 composite. Photocatalyst mass is constant at 50 mg in all experiments.

degradation. Additionally, higher initial BPA concentrations may lead to higher concentrations of degradation products, which may also compete for the active sites on the photocatalyst surface.

On the other hand, Fig. 12b shows that an increase in the initial TET concentration has little effect on TET degradation. For TET, complete degradation is achieved using N-OPK3/T at all initial TET concentrations up to 20 mg $L^{-1}$. The slight decrease in the degradation rate that is observed as the initial TET concentration increases could be due to the absorption of light by the TET molecules. This in turn would reduce the number of photons reaching the photocatalyst surface, which would then reduce the number of ROS generated resulting in a decrease of the overall TET degradation rates.[112] For TET concentrations of 2, 5, and 10 mg $L^{-1}$, about 99.9% removal is achieved after only 10 min. Even at the highest concentration of 20 mg $L^{-1}$, complete removal of TET is achieved after 30 min.

To evaluate the effect of photocatalyst dose, different dosages of T/N-OPK3 were applied. Fig. 13a shows that the lowest BPA degradation rate and efficiency (28%) is observed at a 10 mg catalyst dose in 100 mL of solution (10 mg $L^{-1}$ BPA). The steady increase of photocatalyst dose leads to a quite drastic increase of the degradation efficiencies. This effect has been observed before and has been assigned to an increased number of catalytic sites as the catalyst doses increase.[109] With 100 mg of photocatalyst, 97.5% degradation of BPA is achieved. However, the improvement in BPA degradation between a catalyst dose of 75 and 100 mg is not as large as the improvements observed between the lower doses. This may be due to increased turbidity of the photocatalyst dispersion at higher dosages, which may impede a better photoactivation of the catalyst surface.[113]

Similarly, for TET, increasing the dosage from 10–50 mg enhances the degradation rate, Fig. 13b. With 10 mg of catalyst, the TET degradation rate is slowest, achieving 100% removal in 60 min. In contrast, with doses of 25 or 50 mg, 100% removal of TET is achieved within 30 min.

It is also important to investigate the influence of common matrix species in the aqueous systems on the degradation of pollutant(s). Inorganic anions such as sulphate, bicarbonate, and phosphate are prevalent in surface waters, groundwaters, and wastewaters and can strongly affect the photocatalytic degradation of pollutants. As a result, the effects of these species must be evaluated.

In the case of BPA, typical anions exhibit varying degrees of inhibitory effects on the photocatalytic activity of T/N-OPK3 (Fig. 14a). Bicarbonate and phosphate ions reduce the effective BPA degradation from about 85% (no anions present) to 70% and 59%, respectively. Two plausible explanations for the inhibition of the photocatalytic degradation could be (1) competition of the anions and BPA for the same active sites on the catalyst and (2) scavenging of ROS by bicarbonate ions.[114,115]

Similarly, phosphate may inhibit photocatalysts by a complexation reaction between phosphate and chemical functionalities on the surfaces of the photocatalysts. This may block active sites and hence reduce the efficiency of the

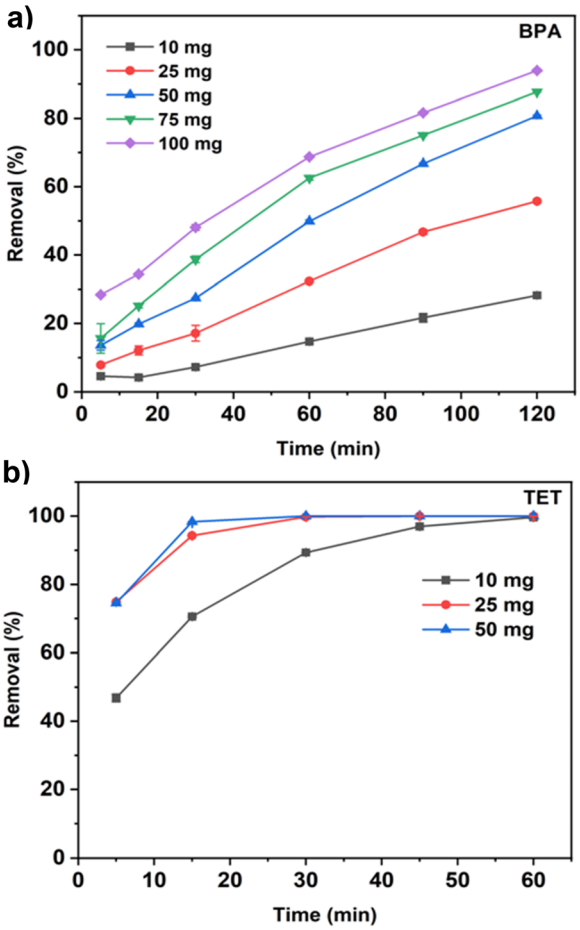


Fig. 13 Effect of catalyst dose on the degradation of (a) BPA and (b) TET *vs.* time using the T/N-OPK3 photocatalyst.

photocatalysts.[49] This is especially important because the concentration of the phosphate in common surface waters (ca. 0.01 M) is much higher than that of BPA (*ca.* 10 mg $L^{-1}$ = 0.04 mM). As a result, phosphate ions are likely a key factor inhibiting the photodegradation of BPA in water bodies.

In contrast, TET photodegradation is not significantly affected by the presence of the anions. This might be due to the fast reaction of the reactive oxygen species with the TET. Likely the good adsorption of TET on the photocatalyst surface provides a very close contact between the ROS generated on the catalyst surface and the adsorbed TET molecules, providing a very effective degradation pathway, see also Fig. 9b.

Moreover, in (waste)water, the presence of $Na^+$ and $Cl^-$ is inevitable. The effect of different NaCl concentrations (0.01, 0.025, and 0.05 M) on the photocatalytic performance of T/N-OPK3 on BPA and TET degradation was therefore evaluated. Fig. 14b demonstrates that NaCl does not inhibit the degradation of either BPA or TET.

Interestingly, in the case of BPA, as the NaCl concentration increases from 0.01 to 0.05 M, a slight increase in the degradation efficiency is observed. This observation is similar to findings by Wang *et al.* who reported that chloride ions can influence degradation in both negative and positive ways either

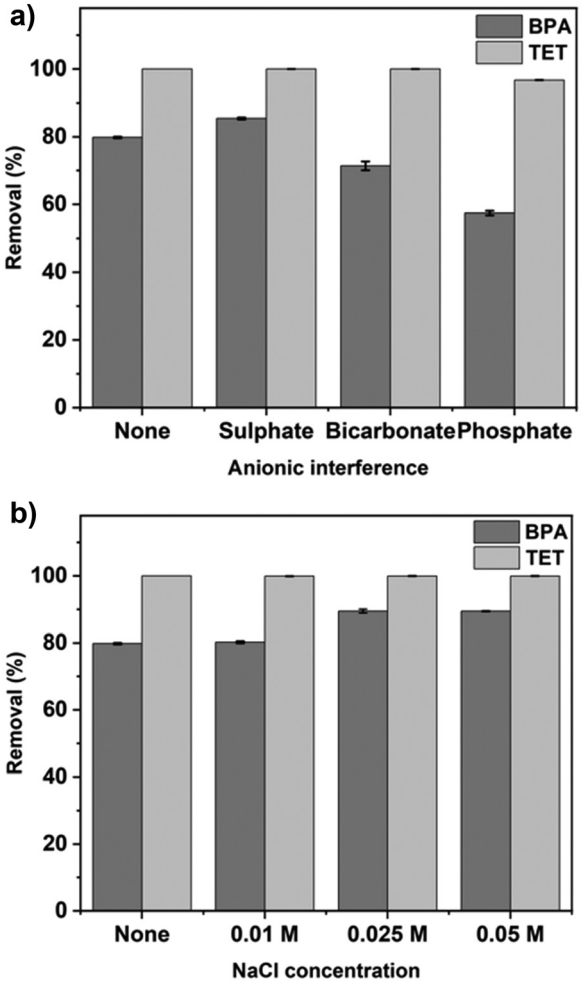


Fig. 14 Effect of (a) anions and (b) ionic strength on the BPA and TET degradation with T/N-OPK3.

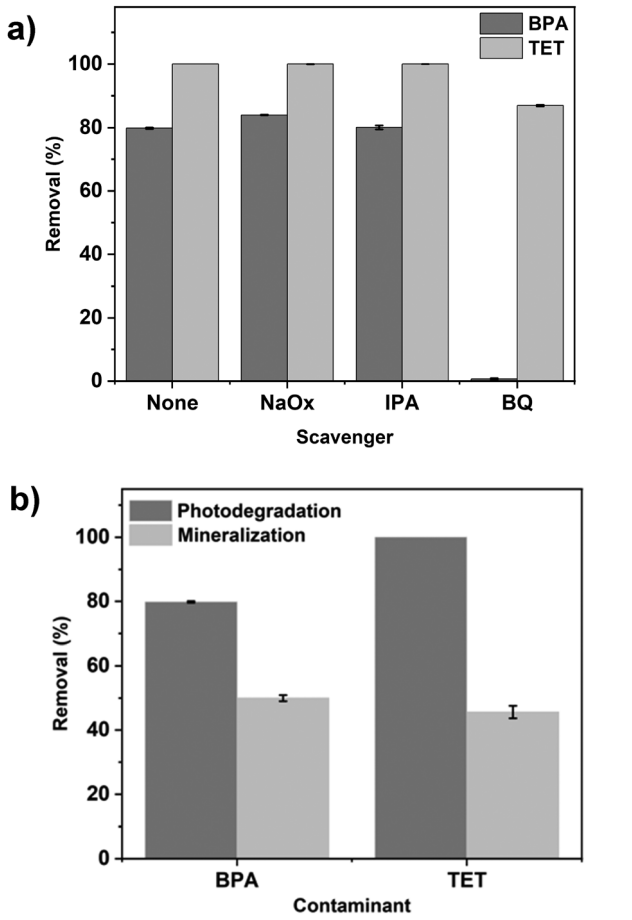


Fig. 15 (a) Effect of different ROS scavengers on the photodegradation of BPA and TET and (b) degree of mineralisation of BPA and TET solutions treated with T/N-OPK3 for 2 h.

by competing with BPA for active sites or by providing more electrons during the photodegradation process. Apparently, negative effects predominate at low chloride concentrations, while positive effects can be more pronounced at higher chloride concentrations.[116]

### 3.4. Effect of scavengers on degradation

To identify the primary ROS responsible for the degradation of both TET and BPA during the photocatalytic process, a series of scavenger experiments were done. In this experiment, isopropyl alcohol (IPA) was chosen as $^{\bullet}OH$ scavenger, benzoquinone (BQ) as $^{\bullet}O_2^-$ scavenger, and sodium oxalate ($NaO_x$) as $h^+$ scavenger. Fig. 15a shows that the addition of $NaO_x$ or IPA does not significantly affect the degradation of TET and BPA. However, BQ significantly reduces the degradation efficiency of T/N-OPK3; it decreases from 100% to 84% for TET and BPA degradation drops from 82% to 5%. This indicates that $^{\bullet}O_2^-$ plays a crucial role in the photocatalytic process by acting as the main oxidizing species generated by the photocatalyst under irradiation, similar to previous studies.[117–119]

### 3.5. Total organic carbon removal efficiency and identification of intermediates

The efficiency of mineralisation (that is, the complete degradation of the contaminants to $CO_2$ and $H_2O$) was evaluated using T/N-OPK3 *via* the determination of the total organic carbon (TOC) levels before and after photocatalysis (Fig. 15b). After 120 min of irradiation, TET and BPA show high degradation rates (100% and 80%, respectively). However, complete mineralisation is not achieved, with TOC removal reaching only 46% for TET and 50% for BPA. This suggests that a substantial portion of the organic carbon remains in solution, either as residual undegraded contaminants or as intermediate byproducts and smaller organic fragments that are resistant to further (photo)oxidation.

This incomplete mineralisation likely at least partly results from insufficient ROS generation. This is possibly caused by surface blockage from adsorbed intermediates leading to reduced photon absorption over time or to a less effective release of the ROS from the photocatalyst surface. Mineralisation efficiency could be improved by extending the irradiation time, optimizing operational variables such as pH or catalyst dosage, or further modifying the catalyst.

 

The intermediates formed in the photocatalytic degradation process using T/N-OPK3 were identified *via* electrospray ionization-liquid chromatography-mass spectrometry (ESI-LC-MS, Fig. S7–S11, SI).

For BPA-containing solutions after the photocatalytic treatment, the primary BPA peak retention time (rt) of 3.34 min and a mass-to-charge ratio (*m/z*) of 227 shows a significant reduction in intensity (Fig. S7, SI). This decrease corroborates the degradation results (Fig. 9a), which indicate that approximately 82% of BPA is removed. However, only one byproduct was detected, with a *m/z* = 257 and rt = 2.96 min (Fig. S9, SI). Given the chosen experimental HPLC setup, the earlier elution (shorter rt) of this intermediate suggests that it is more polar than BPA.

In the case of TET, the primary characteristic peak with a rt = 4.07 min and *m/z* = 445 corresponds to the deprotonated TET molecule ion (Fig. S10, SI). After photodegradation, three main intermediates with *m/z* = 126 (rt = 0.73 min), 168 (rt = 0.73 min), and 236 (rt = 1.16 min) are detected (Fig. S11 and S12, SI).

Overall, the ESI-LC-MS data confirm that complete mineralisation is not achieved within 120 min. Rather, some intermediates form. This is consistent with the TOC analysis (Fig. 15b) showing incomplete mineralisation of both BPA and TET. Table 2 shows the proposed structures of the intermediate products formed in the photocatalytic process for both BPA and TET as inferred from the MS data (Fig. S9–S12, SI).

### 3.6. Proposed mechanism for the photodegradation process

Upon visible-light irradiation, the photocatalyst is photoexcited, generating electron–hole pairs. The photogenerated electrons are transferred to the conduction band and subsequently react with dissolved oxygen to produce superoxide radicals ($^{\bullet}O_2^-$), while the holes in the valence band may participate in oxidation reactions.[127] The efficient separation and transfer of these charge carriers are facilitated by the composite structure of the photocatalyst, which suppresses electron–hole recombination and enhances photocatalytic activity. Trapping experiments using isopropyl alcohol (IPA), benzoquinone (BQ), sodium oxalate (NaOx) as radical scavengers for $^{\bullet}OH$, $^{\bullet}O_2^-$, and $h^+$, respectively, reveal that $^{\bullet}O_2^-$ radicals are likely the dominant reactive species driving the oxidation of BPA and TET (Fig. 15a).

The BPA degradation pathway likely follows an $O_2$-reduction/single electron transfer dominated route through the reduction of $O_2$ to $^{\bullet}O_2^-$ by photogenerated electrons on the catalyst surface. The photoexcited electrons then oxidize BPA *via* single-electron transfer to phenoxyl radicals or peroxy adducts. These species undergo further oxygenation and dehydrogenation to yield oxidized phenolic derivatives such as the quinone-type products (*m/z* = 257, rt 2.96 min) *en route* to mineralisation.[128]

The major byproduct observed in the LC-MS data t (*m/z* = 257, rt 2.96 min) is consistent with previously reported quinone-type oxidation products arising from BPA oxidation, although this assignment is tentative and requires MS/MS/

Table 2 Possible intermediate compounds proposed from the LC-MS analysis of aqueous BPA and TET solutions treated with T/N-OPK3

| Contaminant | rt of intermediate | m/z | Proposed structure of intermediate | Ref |
|---|---|---|---|---|
| Bisphenol A (rt = 3.34 min) (*m/z* = 227) | 2.96 min | 257 | 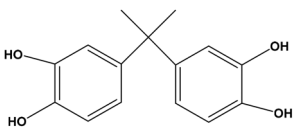 (i) | 120–122 |
| Tetracycline (rt = 4.07 min) (*m/z* = 445) | (i) 0.73 min | (i) 127 | 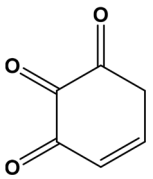 | 123 |
| | (ii) 0.73 min | (ii) 169 | (ii) 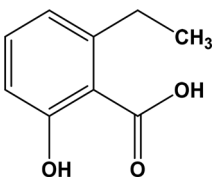 | 123–125 |
| | (iii) 1.16 min | (iii) 236 | (iii) 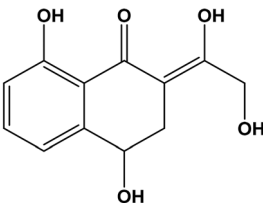 | 126 |

HRMS confirmation. The incomplete mineralisation (TOC ≈ 50% after 120 min) corroborates the presence of persistent polar intermediates and underlines the need for further structural identification and toxicity assessment of the byproducts.

For TET, three intermediates with $m/z$ = 126 (rt = 0.73 min), 168 (rt = 0.73 min), and 236 (rt = 1.16 min) were identified. They likely form *via* successive oxidative cleavage, deamination, dealkylation, and dehydroxylation reactions induced by $^{\bullet}O_2^-$ radicals.[124] The fact that these breakdown products appear at a lower retention times *vs.* the starting TET compound again indicates that they are more hydrophilic than TET. The proposed TET degradation pathway is shown in Fig. S13 (the mechanistic interpretation is based on a combination of direct experimental evidence and literature-supported assignments. The formation of superoxide radicals is supported by scavenger experiments (Fig. 15a), while the degradation intermediates identified by LC-MS provide direct evidence of a possible reaction pathway. Charge carrier generation, electron transfer processes, and the reaction steps are inferred from established photocatalytic mechanisms reported in the literature).

### 3.7. Influence of different water matrices on degradation

Furthermore, the performance of T/N-OPK3 for BPA and TET removal was evaluated across different water matrices: deionized water, tap water, and river water, each spiked with 10 mg $L^{-1}$ of BPA and TET. This assessment provides preliminary insights into the performance of the photocatalyst under conditions that simulate real wastewater environments.

Fig. 16a shows that the photodegradation of BPA is most efficient in deionized water, followed by tap water, and least effective in river water. While the exact reasons for the reduced efficiency are likely rather complex, the generally lower efficiency of the photocatalyst in river water may be attributed to the presence of natural organic matter (NOM) in the river water, as confirmed by TOC analysis (Table S7, SI). Certainly, NOM competes with (organic) pollutants for photocatalyst active sites and scavenges ROS. This competition can lead to reduced catalyst performance over time through fouling.[49]

On the other hand, the overall photodegradation of TET is not influenced by the different water matrices. Complete TET removal even in river water suggests that T/N-OPK3 retains a high photocatalytic activity despite the presence of NOM. While NOM may affect the reaction kinetics, it does apparently not hinder full TET degradation. Therefore, the performance of T/N-OPK3 especially for TET photodegradation in river water shows that T/N-OPK3 holds potential for use in real-world waters (Table 3).

### 3.8. Reusability

One of the key factors that determine the large-scale application of a material in the industry is its ability to be recovered and reused over several cycles without losing its efficiency. Fig. 16b therefore shows the results of a three-cycle reuse experiments with T/N-OPK3 demonstrating that TET degradation is, at least across the three cycles conducted here, essentially unaffected.

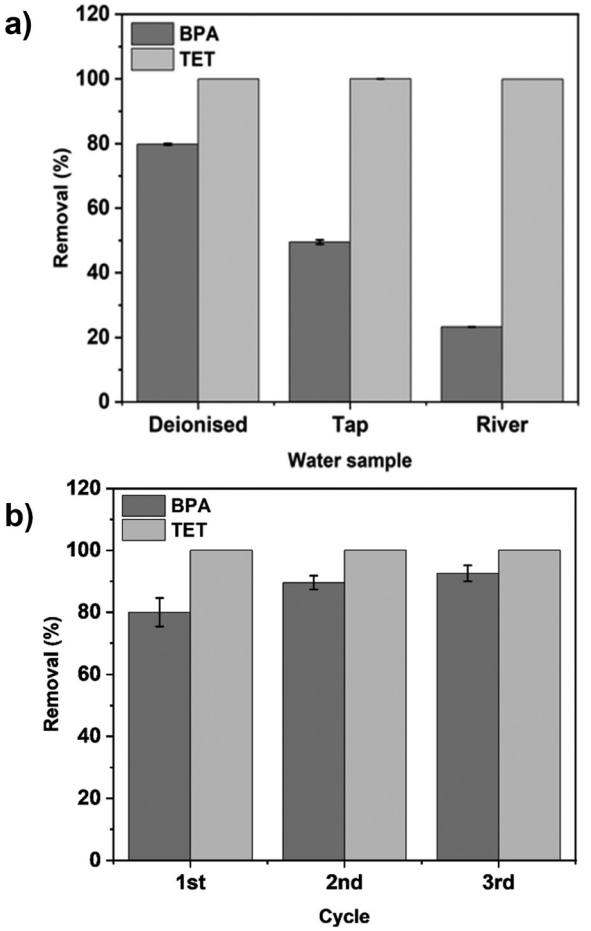


Fig. 16 (a) BPA and TET degradation with T/N-OPK3 in different water matrices and (b) reuse efficiency of T/N-OPK3 for the degradation of BPA and TET. Note that the efficiency with TET is essentially 100% and that the respective error bars in the repeat experiments are extremely small.

Table 3 Removal of BPA and TET in deionized water, tap water, and river water samples with T/N-OPK3. The physicochemical properties of the water matrices used are listed in Table S7, SI

| | Contaminant | |
|---|---|---|
| Water sample | BPA (%) | TET (%) |
| Deionised water | 80 (ND) | 100 (ND) |
| Tap water | 50 (ND) | 100 (ND) |
| River water | 22 (ND) | 100 (ND) |

Values in brackets are the initial concentrations of the contaminant (mg $L^{-1}$) measured in the different water types before spiking with either BPA or TET. ND = not detected.

In contrast, BPA degradation shows an unusual yet reproducible behaviour in that the degradation efficiency of the photocatalyst slightly *increases* from the first to the third cycle. Although no post-use characterization was performed, we hypothesize that this trend may result from the removal of loosely bound surface residues during washing between use. Washing could possibly expose more active sites on the catalyst

 

surface or induce subtle surface modifications which could then slightly enhance BPA adsorption and thus slightly improve degradation. Clearly, further investigation is required to verify this mechanism, but Fig. 16 highlights the potential of T/N-OPK3 for water treatment.

## 4. Comparison of T/N-OPK3 with other $TiO_2$ photocatalyst composites

Table S8 (SI) summarizes the photodegradation performance of T/N-OPK3 *vs.* a series of photocatalysts described in the literature. Specifically, Table S8 shows that T/N-OPK3 is a highly promising and competitive catalyst for the degradation of various organic contaminants. While its degradation efficiency is on par with other catalysts, T/N-OPK3 additionally offers practical advantages, including straightforward synthesis, effective operation with low-energy and low-cost light sources, and good removal efficiency across different classes of pollutants. Although complete mineralisation is not achieved, the level of TOC removal is comparable to literature; among others this finding highlights the need for further investigations into improving the mineralisation efficiency but also demonstrates the that catalysts are competitive in their overall performance.

Relative to a previous photocatalyst,[42] the new T/N-OPK3 shows clear improvements. It exhibits a larger surface area, broader applicability, high reusability, and improved degradation kinetics, particularly for TET in river water. This combination of advantageous properties clearly positions T/N-OPK3 as a potential material for larger scale use in environmental remediation.

## Conclusion

The study presents a facile two-step protocol for producing N-modified hybrid clay photocatalytic composites from orange peel, kaolin clay, melamine, and titania. XPS analysis provides evidence for the presence of $TiO_xN_{1-x}$ in the composites, suggesting that melamine is a nitrogen source for the formation of N-doped titania composite materials. The photocatalysts show an extended optical absorption edge into the visible region, along with a reduced band gap compared to pure titania allowing for the utilization of visible light sources (rather than UV light sources) for photocatalytic degradation of organic pollutants such as tetracycline and bisphenol A in water. The primary mechanism driving the degradation process is the generation of superoxide radicals which then react with the organic pollutants producing a variety of organic fragments. Overall, TOC removal is comparable to existing photocatalysts and the most effective composite T/N-OPK3 exhibits an excellent performance, particularly in the degradation of tetracycline in river water. This highlights its suitability for practical water treatment. Overall, these new hybrid materials present a promising and sustainable alternative for visible light driven removal of a broad range of organic pollutants from water bodies.

## Author contributions

Morenike O. Adesina: conceptualization, methodology, data analysis, visualization, writing – original draft, Moses O. Alfred: writing – review and editing, Harshadrai M. Rawel: investigation, data analysis, writing – review and editing, Christina Günter: investigation, writing – review and editing, Anne Nitschke: investigation, writing – review and editing, Jiyong Kim: investigation, analysis, writing – review and editing. Armin Wedel: analysis, writing – review and editing, Wouter Koopman: investigation, writing – review and editing, Martins O. Omorogie: supervision, writing – review and editing, Emmanuel I. Unuabonah: supervision, writing – review and editing, Andreas Taubert: conceptualization, supervision, writing – review and editing.

## Conflicts of interest

There are no conflicts to declare.

## Data availability

The authors confirm that the data supporting the findings of this study are available within the article and its supplementary information (SI). Supplementary information: Enlarged FT-IR spectra of T/N-OPK2 and T/N-OPK3; $N_2$ adsorption–desorption isotherms and corresponding BJH pore-size distributions of the photocatalyst composites; Tauc plots of the prepared photocatalyst; High-resolution XPS spectra of Al 2p (a) and Si 2p (b) in T/N-OPK3 and OPKT, respectively; high-resolution XPS spectra of C 1s (a) and N 1s (b) in melamine, melam, and melem; Quantitative results of XPS measurements; XPS fitting parameters of the C 1s,N 1s, Ti 2p; reaction scheme of melam and melem from melamine by thermal condensation; the kinetic parameter *vs.* catalyst for the degradation of BPA and TET; direct correlation between surface area of the photocatalysts and rate constant $k$; equilibrium adsorption capacities ($q_e$) of BPA and TET on T/N-OPK catalysts under dark conditions; the extracted ion chromatogram of the LC-MS of the BPA solution before and after degradation using T/N-OPK3; calibration curve employed for Tetracycline and Bisphenol A; the physicochemical properties of the various water matrices; comparison of T/N-OPK3 with other $TiO_2$ photocatalyst composites. See DOI: https://doi.org/10.1039/d6nj00633g.

## Acknowledgements

We thank S. Langen for support with chemicals and supplies, K. Brennenstuhl for UV-DRS analysis, Prof. P. Wessig for loaning the photoreactor setup, and Dr P. Bíró and Prof. S. Oswald for access to the TOC analyzer. We also thank the German Academic Exchange Service (DAAD, Grant No. 57552338, M.O.A.), the Paul and Maria Kremer Foundation (M.O.A.), Deutsche Forschungsgemeinschaft (DFG, German Research Foundation, grant CRC/SFB 1636 – Project ID 510943930 – Project A04 and Project Z01, W.K., A.T.), and the

University of Potsdam (Grant No. 53170000, A.T.) for financial support.

## References

1 R. R. Karri, G. Ravindran and M. H. Dehghani, *Soft computing techniques in solid waste and wastewater management*, Elsevier, 2021, pp. 3–33, DOI: 10.1016/B978-0-12-824463-0.00001-X.
2 A. Saravanan, P. S. Kumar, S. Jeevanantham, S. Karishma, B. Tajsabreen, P. Yaashikaa and B. Reshma, *Chemosphere*, 2021, **280**, 130595.
3 Y. Wang, S. Xue, Y. Liao, Q. Lu, H. Wang, C. Zhao, N. Tang and F. Du, *ACS Appl. Nano Mater.*, 2024, **7**, 3188–3198.
4 G. Moussavi and F. A. Haddad, *Chemosphere*, 2019, **222**, 549–555.
5 Y. Amangelsin, Y. Semenova, M. Dadar, M. Aljofan and G. Bjørklund, *Antibiotics*, 2023, **12**, 440.
6 Z. Wu, Y. Liang, D. Zou, X. Yuan, Z. Xiao, Y. Deng, Y. Zhou, L. Jiang and P. Qin, *J. Environ. Chem. Eng.*, 2020, **8**, 104451.
7 Z. Wu, X. Yuan, H. Zhong, H. Wang, G. Zeng, X. Chen, H. Wang, L. Zhang and J. Shao, *Sci. Rep.*, 2016, **6**, 25638.
8 E. C. Lima, *Ecotoxicol. Environ. Saf.*, 2018, **150**, 1–17.
9 W. Pronk, A. Ding, E. Morgenroth, N. Derlon, P. Desmond, M. Burkhardt, B. Wu and A. G. Fane, *Water Res.*, 2019, **149**, 553–565.
10 M. Kárászová, M. Bourassi and J. Gaálová, *Membranes*, 2020, **10**, 305.
11 M. K. Shahid, A. Kashif, A. Fuwad and Y. Choi, *Coord. Chem. Rev.*, 2021, **442**, 213993.
12 S. Ahmed, M. Mofijur, S. Nuzhat, A. T. Chowdhury, N. Rafa, M. A. Uddin, A. Inayat, T. Mahlia, H. C. Ong and W. Y. Chia, *J. Hazard. Mater.*, 2021, **416**, 125912.
13 H. Wang, Y. Wang and D. D. Dionysiou, *Water*, 2023, **15**, 398.
14 D. Ma, H. Yi, C. Lai, X. Liu, X. Huo, Z. An, L. Li, Y. Fu, B. Li and M. Zhang, *Chemosphere*, 2021, **275**, 130104.
15 O. Aa, J. Zh, G. Bh and A. Ai, *Nanomed. Nanotechnol. Open Access*, 2023, **8**(4), 1–17.
16 M. Mohadesi, M. Sanavi Fard and A. Shokri, *Int. J. Environ. Anal. Chem.*, 2022, 1–22.
17 M. R. Eskandarian, H. Choi, M. Fazli and M. H. Rasoulifard, *Chem. Eng. J.*, 2016, **300**, 414–422.
18 M. B. Tahir, M. Sagir and K. Shahzad, *J. Hazard. Mater.*, 2019, **363**, 205–213.
19 T. Fazal, A. Razzaq, F. Javed, A. Hafeez, N. Rashid, U. S. Amjad, M. S. U. Rehman, A. Faisal and F. Rehman, *J. Hazard. Mater.*, 2020, **390**, 121623.
20 L. Morjène, M. Tasbihi, M. Schwarze, R. Schomäcker, F. Aloulou and M. Seffen, *Water Sci. Technol.*, 2020, **81**, 1882–1893.
21 P. S. Basavarajappa, S. B. Patil, N. Ganganagappa, K. R. Reddy, A. V. Raghu and C. V. Reddy, *Int. J. Hydrogen Energy*, 2020, **45**, 7764–7778.
22 A. Aljaafari, *Curr. Nanosci.*, 2022, **18**, 499–519.
23 A. Meng, L. Zhang, B. Cheng and J. Yu, *Adv. Mater.*, 2019, **31**, 1807660.
24 B. S. Rathi and P. S. Kumar, *Environ. Pollut.*, 2021, **280**, 116995.
25 R. Zouzelka, M. Remzova, J. Plsek, L. Brabec and J. Rathousky, *Catalysts*, 2019, **9**, 708.
26 N. T. Padmanabhan, N. Thomas, J. Louis, D. T. Mathew, P. Ganguly, H. John and S. C. Pillai, *Chemosphere*, 2021, **271**, 129506.
27 A. Balakrishnan, S. Appunni, M. Chinthala and D.-V. N. Vo, *Environ. Chem. Lett.*, 2022, **20**, 3071–3098.
28 M. C. Dlamini, M. S. Maubane-Nkadimeng and J. A. Moma, *J. Environ. Chem. Eng.*, 2021, **9**, 106546.
29 N. Khalid, A. Majid, M. B. Tahir, N. Niaz and S. Khalid, *Ceram. Int.*, 2017, **43**, 14552–14571.
30 M. O. Alfred, M. O. Omorogie, O. Bodede, R. Moodley, A. Ogunlaja, O. G. Adeyemi, C. Günter, A. Taubert, I. Iermak and H. Eckert, *Chem. Eng. J.*, 2020, **398**, 125544.
31 M. O. Adesina, I. Block, C. Günter, E. I. Unuabonah and A. Taubert, *ACS Omega*, 2023, **8**, 21594–21604.
32 S. Mustapha, M. Ndamitso, A. Abdulkareem, J. Tijani, D. Shuaib, A. Ajala and A. Mohammed, *Appl. Water Sci.*, 2020, **10**, 1–36.
33 D. Van Thuan, T. T. H. Chu, H. D. T. Thanh, M. V. Le, H. L. Ngo, C. L. Le and H. P. Thi, *Environ. Res.*, 2023, **236**, 116789.
34 J. S. Lazarotto, V. de Lima Brombilla, S. Silvestri and E. L. Foletto, *Appl. Organomet. Chem.*, 2020, **34**, e6001.
35 H. Ashebir, S. Babaee, A. Worku, P. Diale, T. Msagati and J. F. Nure, *Sci. Rep.*, 2025, **15**, 31795.
36 A. Piątkowska, M. Janus, K. Szymański and S. Mozia, *Catalysts*, 2021, **11**, 144.
37 M. Nasirian, Y. Lin, C. Bustillo-Lecompte and M. Mehrvar, *Int. J. Environ. Sci. Technol.*, 2018, **15**, 2009–2032.
38 M. Ocampo-Gaspar, C. Rosiles-Pérez, K. Torres-Nava, L. Aleman-Capistran and A. Jiménez-González, *J. Mater. Sci.: Mater. Eng.*, 2025, **20**, 77.
39 P. Lian, A. Qin, Z. Liu, H. Ma, L. Liao, K. Zhang and Y. Qin, *Materials*, 2025, **18**, 2400.
40 M. Mohtaram, S. Mohtaram, S. Sabbaghi, X. You, W. Wu, L. Jia, K. Muzammil, N. Alraee, S. Islam and Y. Aryanfar, *J. Water Process Eng.*, 2024, **58**, 104884.
41 Y. Sun, Y. Ahmadi and K.-H. Kim, *Environ. Res.*, 2024, **260**, 119664.
42 M. O. Adesina, M. O. Alfred, H. Seitz, K. Brennenstuhl, H. M. Rawel, P. Wessig, J. Kim, A. Wedel, W. Koopman and C. Günter, *Environ. Sci.: Water Res. Technol.*, 2024, **10**, 1432–1450.
43 E. Bayat, M. Ströbele, D. Enseling, T. Jüstel and H.-J. Meyer, *Dalton Trans.*, 2024, **53**, 10912–10918.
44 M. Amer and A. Elwardany, *Renewable energy-resources, challenges and applications*, IntechOpen, 2020.
45 P. Makuła, M. Pacia and W. Macyk, *ACS Nano*, 2018, **9**, 6814–6817.
46 N. K. Swamy, K. N. S. Mohana and S. R. Yashas, *Colloids Surf., A*, 2022, **639**, 128324.

 

47 R. H. A. Murti, M. A. S. Jawwad, K. K. Ayuningtiyas and E. N. Hidayah, *S. Afr. J. Chem. Eng.*, 2025, **53**(1), 87–95.
48 R. Yang, B. Liang, S. Zheng, C. Hu, Y. Xu, Y. Ma, Y. Bai, K. Dai, Y. Tang and C. Zhang, *Arabian J. Chem.*, 2023, **16**, 104397.
49 A. A. Bayode, E. M. Vieira, R. Moodley, S. Akpotu, A. S. de Camargo, D. Fatta-Kassinos and E. I. Unuabonah, *Chem. Eng. J.*, 2021, **420**, 127668.
50 E. I. Unuabonah, A. Adewuyi, M. O. Kolawole, M. O. Omorogie, O. C. Olatunde, S. O. Fayemi, C. Günter, C. P. Okoli, F. O. Agunbiade and A. Taubert, *Heliyon*, 2017, **3**, e00379.
51 A. O. Egbedina, K. O. Adebowale, B. I. Olu-Owolabi, E. I. Unuabonah and M. A. Adeyemo, *Arabian J. Sci. Eng.*, 2022, **47**, 5755–5765.
52 J. C. Colmenares, R. S. Varma and P. Lisowski, *Green Chem.*, 2016, **18**, 5736–5750.
53 M. El-Azazy, A. S. El-Shafie and K. Al-Saad, *Infrared spectroscopy-perspectives and applications*, IntechOpen, 2022.
54 H. Zhu and S.-a Xu, *RSC Adv.*, 2018, **8**, 17879–17887.
55 P. Monji, R. Jahanmardi and M. Mehranpour, *Carbon Lett.*, 2018, **27**, 81–89.
56 B. Ren, T. Wang, G. Qu, F. Deng, D. Liang, W. Yang and M. Liu, *Environ. Sci. Pollut. Res.*, 2018, **25**, 19122–19133.
57 C. Kuntz, C. Kuhn, H. Weickenmeier, S. Tischer, M. Börnhorst and O. Deutschmann, *Chem. Eng. Sci.*, 2021, **246**, 116876.
58 H.-Y. Xu, L.-C. Wu, H. Zhao, L.-G. Jin and S.-Y. Qi, *PLoS One*, 2015, **10**, e0142616.
59 Y. Hong, L. Wang, E. Liu, J. Chen, Z. Wang, S. Zhang, X. Lin, X. Duan and J. Shi, *Inorg. Chem. Front.*, 2020, **7**, 347–355.
60 J. Gomes, J. Lincho, E. Domingues, R. M. Quinta-Ferreira and R. C. Martins, *Water*, 2019, **11**, 373.
61 M. Roškarič, G. Žerjav, M. Finšgar, J. Zavašnik and A. Pintar, *J. Alloys Compd.*, 2023, **947**, 169585.
62 S. Shahzadi, S. Zaheer, K. Bakht, F. Verpoort, H. Ullah and H. Y. Kim, *Mater. Today Sustain.*, 2025, 101192.
63 Y. Zhang, Q. Pan, G. Chai, M. Liang, G. Dong, Q. Zhang and J. Qiu, *Sci. Rep.*, 2013, **3**, 1–8.
64 R. Abazari, A. R. Mahjoub and S. Sanati, *RSC Adv.*, 2014, **4**, 56406–56414.
65 M. Li, H. Miura and T. Shishido, *Energy Fuels*, 2024, **38**, 10050–10061.
66 X. Zeng, X. Sun and Y. Wang, *Environ. Eng. Res.*, 2021, **26**(6), 200524.
67 M. R. Islam, A. K. Chakraborty, M. Gafur, M. A. Rahman and M. H. Rahman, *Res. Chem. Intermed.*, 2019, **45**, 1753–1773.
68 C. Li, Z. Sun, W. Zhang, C. Yu and S. Zheng, *Appl. Catal., B*, 2018, **220**, 272–282.
69 M. M. Rahman, A. Z. Shafiullah, A. Pal, M. A. Islam, I. Jahan and B. B. Saha, *Energies*, 2021, **14**, 7478.
70 S. A. El-Sayed, T. M. Khass and M. E. Mostafa, *Biomass Convers. Biorefin.*, 2024, **14**, 17779–17803.
71 R. Deju, A. Cucos, M. Mincu and C. Tuca, *Rom. J. Phys.*, 2021, **66**, 1–8.
72 B. C. Y. Lee, F. Y. Lim, W. H. Loh, S. L. Ong and J. Hu, *Water*, 2021, **13**, 2340.
73 F. Rizzi, R. Castaldo, T. Latronico, P. Lasala, G. Gentile, M. Lavorgna, M. Striccoli, A. Agostiano, R. Comparelli and N. Depalo, *Molecules*, 2021, **26**, 4247.
74 E. A. Al-Maliky, H. A. Gzar and M. G. Al-Azawy, *IOP Conf. Ser.: Mater. Sci. Eng.*, 2021, **1184**, 012004.
75 M. Kosmulski, *Adv. Colloid Interface Sci.*, 2023, 102973.
76 H. Liao and T. Reitberger, *Catalysts*, 2013, **3**, 418–443.
77 M. Kaneko, *Heliyon*, 2019, **5**, 5.
78 E. Apaydın Varol and Ü. Mutlu, *Energies*, 2023, **16**, 3674.
79 P. V. Bakre, S. Tilve and R. Shirsat, *Arabian J. Chem.*, 2020, **13**, 7637–7651.
80 P. Ganguly, M. Muscetta, N. T. Padmanabhan, L. Clarizia, A. Akande, S. Hinder, S. Mathew, H. John, A. Breen and S. C. Pillai, *Appl. Catal., B*, 2021, **282**, 119612.
81 J. Ma, W. Li, N. T. Le, J. A. Díaz-Real, M. Body, C. Legein, J. Swiatowska, A. Demortière, O. J. Borkiewicz and E. A. Konstantinova, *ACS Omega*, 2019, **4**, 10929–10938.
82 W. Zhang, N. Li, P. Wu, D. Wang, P. Dong and Y. Zhao, *ChemistrySelect*, 2023, **8**, e202204826.
83 Q. Raza, I. Bibi, F. Majid, S. Kamal, S. Ata, A. Ghafoor, M. I. Arshad, S. H. Al-Mijalli, A. Nazir and M. Iqbal, *J. Ind. Eng. Chem.*, 2023, **118**, 469–482.
84 S. Lettieri, M. Pavone, A. Fioravanti, L. Santamaria Amato and P. Maddalena, *Materials*, 2021, **14**, 1645.
85 W. Zhou and H. Fu, *Inorg. Chem. Front.*, 2018, **5**, 1240–1254.
86 R. Jaiswal, J. Bharambe, N. Patel, A. Dashora, D. Kothari and A. Miotello, *Appl. Catal., B*, 2015, **168**, 333–341.
87 E. O. Oseghe and A. E. Ofomaja, *J. Environ. Manage.*, 2018, **223**, 860–867.
88 T. L. Barr and S. Seal, *J. Vac. Sci. Technol., A*, 1995, **13**, 1239–1246.
89 M. C. Biesinger, *Appl. Surf. Sci.*, 2022, **597**, 153681.
90 P. Stoyanov, S. Akhter and J. White, *Surf. Interface Anal.*, 1990, **15**, 509–515.
91 P. Lin, Y. Zhang, Z. Cui, R. Xiong, C. Wen, B. Wu, Q. Lin and B. Sa, *Materials*, 2022, **15**, 7312.
92 M. Nielsen, A. Hafreager, R. Y. Brogaard, K. De Wispelaere, H. Falsig, P. Beato, V. Van Speybroeck and S. Svelle, *Catal. Sci. Technol.*, 2019, **9**, 3721–3725.
93 N. Liu, T. Li, Z. Zhao, J. Liu, X. Luo, X. Yuan, K. Luo, J. He, D. Yu and Y. Zhao, *ACS Omega*, 2020, **5**, 12557–12567.
94 O. Diwald, T. L. Thompson, T. Zubkov, E. G. Goralski, S. D. Walck and J. T. Yates, *J. Phys. Chem. B*, 2004, **108**, 6004–6008.
95 C. Chen, H. Bai and C. Chang, *J. Phys. Chem. C*, 2007, **111**, 15228–15235.
96 X. Chen, Y. B. Lou, A. C. Samia, C. Burda and J. L. Gole, *Adv. Funct. Mater.*, 2005, **15**, 41–49.
97 X. Chen and C. Burda, *J. Phys. Chem. B*, 2004, **108**, 15446–15449.
98 J. F. Watts and J. Wolstenholme, *An introduction to surface analysis by XPS and AES*, John Wiley & Sons, 2019.

99 Z. Xu, S. Gu, Z. Sun, D. Zhang, Y. Zhou, Y. Gao, R. Qi and W. Chen, *Environ. Sci. Pollut. Res.*, 2020, **27**, 11012–11025.
100 S. Dyjak, W. Kiciński and A. Huczko, *J. Mater. Chem. A*, 2015, **3**, 9621–9631.
101 J. B. Yoo, H. J. Yoo, H. J. Jung, H. S. Kim, S. Bang, J. Choi, H. Suh, J.-H. Lee, J.-G. Kim and N. H. Hur, *J. Mater. Chem. A*, 2016, **4**, 869–876.
102 M. Kuznetsov, J. F. Zhuravlev, V. Zhilyaev and V. Gubanov, *J. Electron Spectrosc. Relat. Phenom.*, 1992, **58**, 1–9.
103 T. Sakata, S. Ogawa, K. Inoue, Y. Shimizu and Y. Tanahashi, *Surf. Interface Anal.*, 2022, **54**, 661–666.
104 A. Von Richthofen and R. Domnick, *Thin Solid Films*, 1996, **283**, 37–44.
105 M. C. Biesinger, University of South Australia, 2012.
106 N. Kovalevskiy, D. Svintsitskiy, S. Cherepanova, S. Yakushkin, O. Martyanov, S. Selishcheva, E. Gribov, D. Kozlov and D. Selishchev, *Nanomaterials*, 2022, **12**, 4146.
107 C. Huang, N. Fang, W. Yu, R. Wang, Y. Chu and J. Li, *J. Ind. Eng. Chem.*, 2024, DOI: 10.1016/j.jiec.2024.07.041.
108 X. Wang and T.-T. Lim, *Appl. Catal., B*, 2010, **100**, 355–364.
109 Y. Hunge, A. Yadav, S. Khan, K. Takagi, N. Suzuki, K. Teshima, C. Terashima and A. Fujishima, *J. Colloid Interface Sci.*, 2021, **582**, 1058–1066.
110 Y. Fu, L. Peng, Q. Zeng, Y. Yang, H. Song, J. Shao, S. Liu and J. Gu, *Chem. Eng. J.*, 2015, **270**, 631–640.
111 M. Ahmadi, H. R. Motlagh, N. Jaafarzadeh, A. Mostoufi, R. Saeedi, G. Barzegar and S. Jorfi, *J. Environ. Manage.*, 2017, **186**, 55–63.
112 G. Safari, M. Hoseini, M. Seyedsalehi, H. Kamani, J. Jaafari and A. Mahvi, *Int. J. Environ. Sci. Technol.*, 2015, **12**, 603–616.
113 S. L. Prabavathi, K. Saravanakumar, C. M. Park and V. Muthuraj, *Sep. Purif. Technol.*, 2021, **257**, 117985.
114 J. Jia, D. Liu, S. Wang, H. Li, J. Ni, X. Li, J. Tian and Q. Wang, *Sep. Purif. Technol.*, 2020, **253**, 117510.
115 X. Cheng, L. Liang, J. Ye, N. Li, B. Yan and G. Chen, *Sci. Total Environ*, 2023, 164086.
116 Z. Wang, R. Yuan, Y. Guo, L. Xu and J. Liu, *J. Hazard. Mater.*, 2011, **190**, 1083–1087.
117 I. Altin, *J. Mol. Struct.*, 2022, **1252**, 132199.
118 D. Li, X. Zhang and W. Zhang, *Chem. Eng. J.*, 2021, **405**, 126867.
119 Y. Huang, S. Kou, X. Zhang, L. Wang, P. Lu and D. Zhang, *Nanomaterials*, 2020, **10**, 724.
120 T. Ahamad, M. Naushad, Y. Alzaharani and S. M. Alshehri, *J. Mol. Liq.*, 2020, **311**, 113339.
121 C. Zhao, J. Wang, X. Chen, Z. Wang, H. Ji, L. Chen, W. Liu and C.-C. Wang, *Sci. Total Environ*, 2021, **752**, 141901.
122 M. Deng, L. Wang, Z. Wen, J. Chakraborty, J. Sun, G. Wang and P. Van Der Voort, *Green Chem.*, 2024, **26**, 3239–3248.
123 X. Chen, H. Zhang, S. Xu, X. Du, K. Zhang, C.-P. Hu, S. Zhan, X. Mi, W. D. Oh and X. Hu, *Catalysts*, 2023, **13**, 1150.
124 L. Wang, R. Li, Y. Zhang, Y. Gao, X. Xiao, Z. Zhang, T. Chen and Y. Zhao, *RSC Adv.*, 2023, **13**, 6368–6377.
125 D. Jia, Y. Zhang, X. Zhang, P. Feng, L. Yang, R. Ning, H. Pan and Y. Miao, *Environ. Sci.: Nano*, 2021, **8**, 415–431.
126 K.-P. Cui, T.-T. Yang, Y.-H. Chen, R. Weerasooriya, G.-H. Li, K. Zhou and X. Chen, *Environ. Technol.*, 2022, **43**, 3341–3354.
127 Q. Raza, G. Fatima, B. Lu, I. Bibi, J. An and S. Lim, *Surf. Interfaces*, 2025, 107203.
128 Q. Han, M. Wang, F. Sun, B. Yu, Z. Dong, P. Li, J. Luo, M. Li, X. Jin and Z. Dai, *Environ. Res.*, 2023, **216**, 114601.

 